Sympathetic neuron–associated macrophages contribute to obesity by importing and metabolizing norepinephrine

Roksana M Pirzgalska[1,11], Elsa Seixas[1,11], Jason S Seidman[2], Verena M Link[2,3], Noelia Martínez Sánchez[1], Inês Mahú[1], Raquel Mendes[1], Vitka Gres[1], Nadiya Kubasova[1], Imogen Morris[1], Bernardo A Arús[1,4], Chelsea M Larabee[1], Miguel Vasques[1,5], Francisco Tortosa[6], Ana L Sousa[7], Sathyavathy Anandan[1], Erin Tranfield[7], Maureen K Hahn[8], Matteo Iannacone[9], Nathanael J Spann[2], Christopher K Glass[2] & Ana I Domingos[1,10]

The cellular mechanism(s) linking macrophages to norepinephrine (NE)-mediated regulation of thermogenesis have been a topic of debate. Here we identify sympathetic neuron–associated macrophages (SAMs) as a population of cells that mediate clearance of NE via expression of solute carrier family 6 member 2 (SLC6A2), an NE transporter, and monoamine oxidase A (MAOA), a degradation enzyme. Optogenetic activation of the sympathetic nervous system (SNS) upregulates NE uptake by SAMs and shifts the SAM profile to a more proinflammatory state. NE uptake by SAMs is prevented by genetic deletion of *Slc6a2* or inhibition of the encoded transporter. We also observed an increased proportion of SAMs in the SNS of two mouse models of obesity. Genetic ablation of *Slc6a2* in SAMs increases brown adipose tissue (BAT) content, causes browning of white fat, increases thermogenesis, and leads to substantial and sustained weight loss in obese mice. We further show that this pathway is conserved, as human sympathetic ganglia also contain SAMs expressing the analogous molecular machinery for NE clearance, which thus constitutes a potential target for obesity treatment.

Sympathetic innervation of adipose tissue promotes lipolysis and fat mass reduction via NE signaling[1]. In obesity, chronic local inflammation underlies adipose tissue dysfunction, and macrophages have been shown to play a central role[1,2]. The mechanism that links macrophages in white adipose tissue (WAT) to NE remains controversial. Some groups have reported that anti-inflammatory adipose tissue macrophages (ATMs) in the WAT produce NE to sustain thermogenesis and browning. In direct contradiction, other groups have reported that ATMs do not express a key enzyme required for NE production and that genetic deletion of this enzyme in mouse macrophages has no effect on thermogenesis and body weight[3–6].

Here we identify a previously undescribed population of SAMs that import and degrade NE via specific proteins that are absent from ATMs. We found by transcriptional profiling of isolated SAMs that neural- and adrenergic-related genes are differentially expressed in these cells relative to other macrophage populations. SAMs accumulate intracellular NE despite lacking enzymes for NE biosynthesis. Using optogenetics, we demonstrate that SNS activity increases NE content and the proinflammatory state of SAMs. We functionally demonstrate that SAMs import and degrade NE via NE transporter (SLC6A2) and degradation enzyme (MAOA), respectively. We further demonstrate that SAM-mediated clearance of extracellular NE contributes to obesity, as inhibiting NE import by SAMs ameliorates obesity, thermogenesis, and browning in mutant obese (*ob*/*ob*) mice and mice fed a high-fat diet (HFD). Finally, we demonstrate human relevance for this mechanism, as we found that SAMs are also present in human sympathetic ganglia and express similar molecular machinery as that observed in mice. Thus, the identification of SAMs represents a new contribution to the ongoing controversy surrounding the role of macrophages in thermogenesis and obesity while identifying an unforeseen immunological player in noradrenergic homeostasis with therapeutic potential for obesity.

RESULTS

Specialized morphology and activation of SNS *Cx3cr1*-expressing cells

Our initial aim was to visualize the *in vivo* morphology of ATMs using two-photon and confocal microscopy in *Cx3cr1*$^{GFP/+}$ mice, in which macrophages are labeled with GFP. ATMs in fat parenchyma had a regular circular shape (**Fig. 1a**), whereas those located on sympathetic

[1]The Howard Hughes Medical Institute (HHMI) and Obesity Laboratory, Instituto Gulbenkian de Ciência, Oeiras, Portugal. [2]Department of Cellular and Molecular Medicine, University of California, San Diego, La Jolla, California, USA. [3]Faculty of Biology, Department II, Ludwig-Maximilians Universität München, Planegg-Martinsried, Germany. [4]Departamento de Bioquímica, Instituto de Ciências Básicas da Saúde, Universidade Federal do Rio Grande do Sul, Porto Alegre, Brazil. [5]Department of Endocrinology, Curry Cabral Hospital, Centro Hospitalar de Lisboa Central, Lisbon, Portugal. [6]Department of Pathology, Centro Hospitalar Lisboa Norte, Hospital de Santa Maria, EPE, Lisbon, Portugal. [7]Electron Microscopy Unit, Instituto Gulbenkian de Ciência, Oeiras, Portugal. [8]Vanderbilt Kennedy Center for Research on Human Development, Vanderbilt University School of Medicine, Nashville, Tennessee, USA. [9]Division of Immunology, Transplantation and Infectious Diseases, Istituto di Ricovero e Cura a Carattere Scientifico (IRCCS) San Raffaele Scientific Institute, Milan, Italy. [10]The Howard Hughes Medical Institute (HHMI), New York, New York, USA. [11]These authors contributed equally to this work. Correspondence should be addressed to A.I.D. (dominan@igc.gulbenkian.pt).

Received 6 May; accepted 12 September; published online 9 October 2017; doi:10.1038/nm.4422

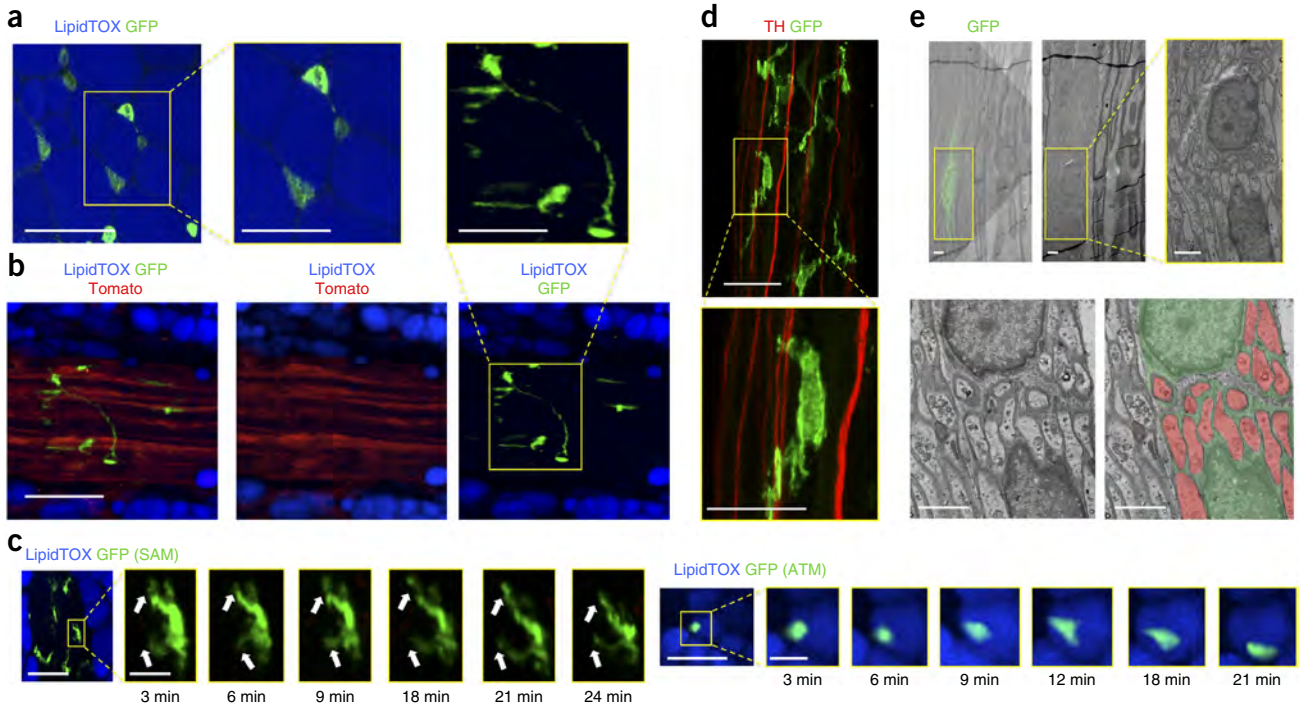

Figure 1 Sympathetic neuron–associated *Cx3cr1*-GFP$^+$ cells exhibit differentiated morphology for specific association with SNS neurons. (**a**) Confocal images of WAT isolated from a *Cx3cr1*$^{GFP/+}$ mouse and stained using lipid stain LipidTOX (blue) and anti-GFP antibody (green). Images are representative of five similar experiments. (**b**) Confocal images of sympathetic nerve fibers in subcutaneous adipose tissue isolated from a cross of *TH-cre*; *LSL-Tomato* (red) and *Cx3cr1*$^{GFP/+}$ (green) mice. Adipocytes were stained using lipid stain LipidTOX (blue). Images are representative of three similar experiments. Scale bars in **a** and **b**, 50 μm. The boxed regions in the main micrographs in **a** and **b** are shown at higher magnification; scale bars, 25 μm. (**c**) Intravital multiphoton visualization of a neural–adipose connection in the inguinal fat pad of a live *Cx3cr1*$^{GFP/+}$ mouse; LipidTOX (blue) labels adipocytes. Images depict the morphological features and cell dynamics of *Cx3cr1*-GFP$^+$ cells associated with sympathetic nerve fibers (left) and *Cx3cr1*-GFP$^+$ cells in the parenchyma of subcutaneous fat (right). Images are representative of three similar experiments. Scale bars, 50 μm. Boxed regions in the main micrographs are shown at higher magnification at the indicated time points; scale bars, 10 μm. White arrows indicate dendritiform processes over time. (**d**) Confocal images of sympathetic nerve fibers isolated from the inguinal fat pad of a *Cx3cr1*$^{GFP/+}$ mouse and stained using anti-TH (red) and anti-GFP (green) antibodies. Images are representative of five similar experiments. Scale bar, 50 μm. The boxed region in the main micrograph is shown at higher magnification below; scale bar, 25 μm. (**e**) Correlative confocal and transmission electron microscopy of nerve fibers isolated from the subcutaneous fat pad of a *Cx3cr1*$^{GFP/+}$ mouse. Shown are an overlay of the GFP fluorescence (green) with the electron micrograph of the same section (upper left; the lower left image is a higher-magnification view of the boxed region), the electron micrograph alone (upper middle; the yellow boxed region is shown at higher magnification to the right), and the electron micrograph from the lower left with false coloring highlighting *Cx3cr1*-GFP$^+$ cells (green) and sympathetic nerves (red) (lower right). Images are representative of two similar experiments. Scale bars, 2 μm.

nerve bundles exhibited profuse pseudopodia that extended over a greater surface area (**Fig. 1b** and **Supplementary Fig. 1a**,**b**). Furthermore, we observed that sympathetic neuron–associated *Cx3cr1*-GFP$^+$ cells displayed dynamic extensions and retractions of dendritiform processes over time (**Fig. 1c** and **Supplementary Video 1**). In contrast, ATMs surrounding adipocytes displayed minimal temporal plasticity or displacement (**Fig. 1c** and **Supplementary Video 2**). Using correlative light–electron microscopy on WAT-derived nerve bundles, we confirmed that *Cx3cr1*-GFP$^+$ cells extended thin pseudopodial processes that enveloped nonmyelinated SNS axons (**Fig. 1d**,**e** and **Supplementary Fig. 1c**).

We then investigated whether sympathetic neuron–associated *Cx3cr1*-GFP$^+$ cells were present in other SNS compartments, such as paravertebral sympathetic ganglia. Through imaging superior cervical ganglia (SCGs) and thoracic chains, we visualized *Cx3cr1*-GFP$^+$ cells that were morphologically similar to those within WAT-derived SNS bundles (**Supplementary Fig. 2**). Owing to the established *ex vivo* explant potential of SCGs, we used them along with WAT-derived SNS nerve bundles as model systems for subsequent functional and molecular analyses.

SNS *Cx3cr1*-expressing SAMs exhibit hematopoietic characteristics

Because nearly all *Cx3cr1*-GFP$^+$ cells isolated from sympathetic fibers expressed the immune marker CD45 (**Supplementary Fig. 3**) and macrophage marker F4/80 (**Supplementary Fig. 4a**), we designated these cells SAMs. Because of the specialized morphology and location of SAMs, we next explored how these cells compared to other tissue macrophages and brain microglia. We sorted F4/80$^+$CD45$^+$ cells from the following tissues: sympathetic ganglia (SAM ganglia), sympathetic nerve fibers from inguinal fat (SAM fibers), neighboring subcutaneous fat (sATM), visceral fat (vATM), spleen (SpM), and brain (microglia) (**Fig. 2a**; gating details in **Supplementary Fig. 3**). The relative abundance of CD45^{high}*Cx3cr1*-GFP$^+$ cells was nearly four times higher within nerve fibers (SAMs) than in subcutaneous WAT (sWAT) (sATMs; **Supplementary Fig. 4b**).

CD45 is highly expressed in hematopoietic cells but expressed at low levels in microglia. Flow cytometric analysis revealed that SAMs are CD45^{medium} or CD45^{high} (**Supplementary Fig. 3**), suggesting a hematopoietic origin for these cells. To test this hypothesis, we generated chimeras through transplantation of bone marrow from

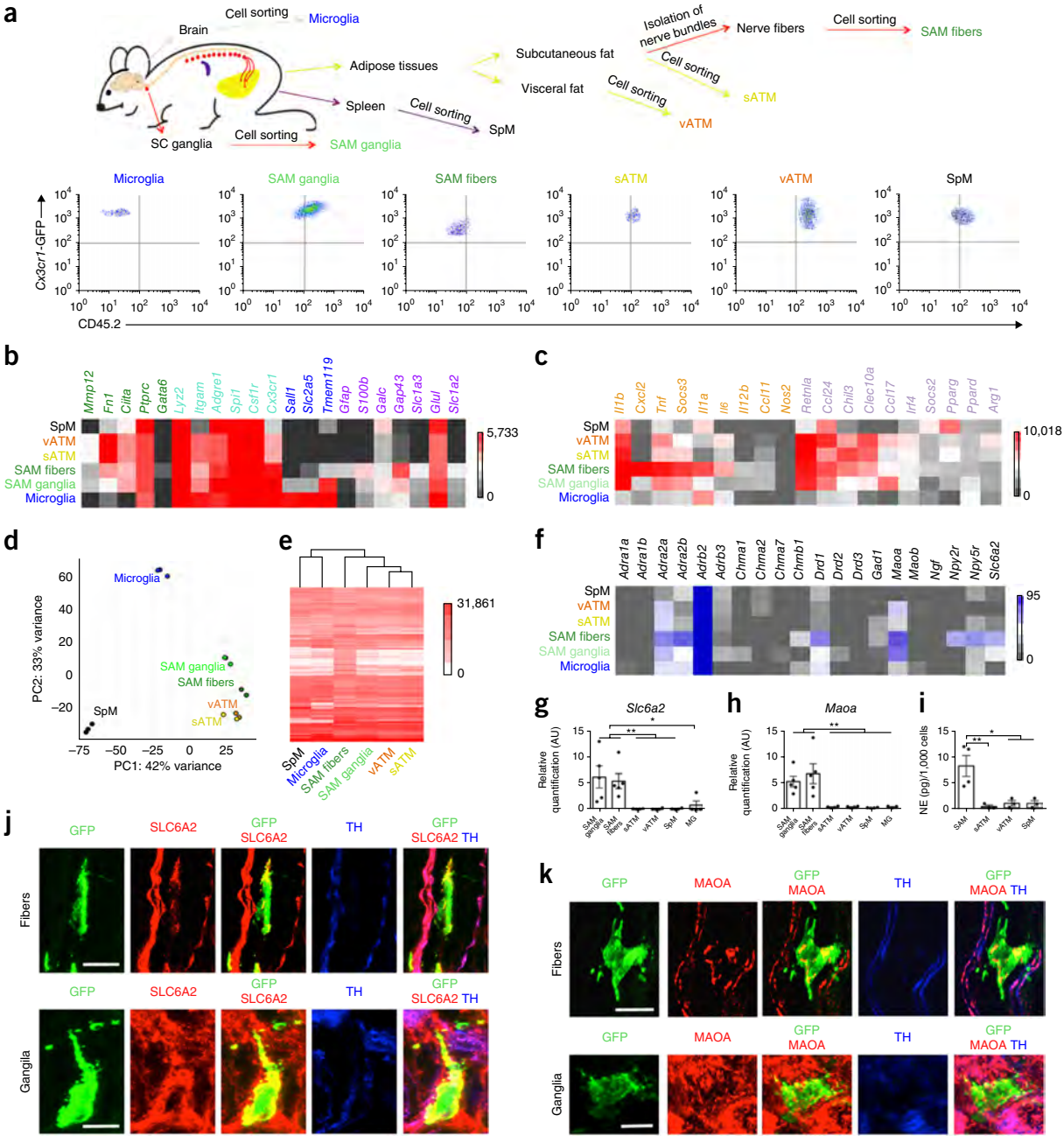

Figure 2 SAMs highly express macrophage-associated markers and possess the machinery for uptake and degradation of norepinephrine. (**a**) Top, schematic representation of tissue dissections and processing of macrophages isolated from the following tissues: brain, spleen, visceral fat, subcutaneous fat, sympathetic nerve fibers from subcutaneous fat, and superior cervical ganglia (SC ganglia). Bottom, representative flow cytometry dot plots indicating the CD45.2 status of macrophages from each tissue analyzed. (**b**) Heat map showing expression of genes associated with macrophage (green and cyan), microglial (blue and cyan), and glial (purple) profiles as determined by low-input RNA-seq. Values are in reads per kilobase of transcript per million mapped reads (RPKM). (**c**) Heat map showing expression of proinflammatory (orange) and anti-inflammatory (purple) genes as determined by low-input RNA-seq. Values are in RPKM. (**d**) PCA based on the top 500 genes with the most variable expression across SAM fibers (green), SAM ganglia (light green), vATM (orange), sATM (yellow), SpM (black), and microglia (blue). Each dot represents an independent experiment. (**e**) Heat map of transcript levels (RPKM values) based on the 5,000 genes most highly expressed by SAM fibers as determined by low-input RNA-seq. (**f**) Heat map showing expression of genes encoding neurotransmitter receptors, transporters, and catalytic enzymes. RPKM values were determined by low-input RNA-seq. Values in **b**–**f** represent three (SpM, microglia, and SAM ganglia) or two (vATM, sATM, and SAM fibers) independent experiments. (**g**) Expression of mRNA for *Slc6a2* as determined by qRT–PCR presented with normalization to *Gapdh* expression. Each data point represents tissues pooled from ten mice. $n = 5$ experiments for SAM fibers and SAM ganglia and $n = 4$ experiments for SpM, vATM, sATM, and microglia (MG). (**h**) Expression of mRNA for *Maoa* as determined by qRT–PCR with normalization to *Gapdh* expression. Each data point represents tissues pooled from ten mice. $n = 5$ experiments for SAM fibers and SAM ganglia, $n = 4$ experiments for SpM, vATM, and sATM, and $n = 3$ experiments for microglia. (**i**) NE content in sorted CD45.2 (PE)$^+$F4/80 (Alexa Fluor 647)$^+$ cells measured by NE ELISA. The numbers of cells used in NE assays were as follows: 858 ± 258 for SAMs ($n = 4$ experiments) and 1,000 cells for sATMs, vATMs, and SpMs ($n = 3$ experiments). (**j**,**k**) Confocal images of sympathetic nerve fibers (top) and SCG (bottom) isolated from *Cx3cr1*$^{GFP/+}$ mice and stained using anti-GFP (green) and anti-TH (blue) antibodies together with anti-SLC6A2 (**j**) or anti-MAOA (**k**) antibody (red). Images are representative of two experiments. Scale bars, 10 µm. Data in **g**–**i** were analyzed by one-way ANOVA followed by Tukey's multiple-comparisons test. Data are shown as average ± s.e.m. $^*P < 0.05$, $^{**}P < 0.01$.

CD45.2 *Cx3cr1*$^{GFP/+}$ donors into irradiated CD45.1 recipient mice and observed complete repopulation of CD45$^+$ cells derived from the CD45.2 *Cx3cr1*$^{GFP/+}$ donors (**Supplementary Fig. 4c**). Eight weeks following transplantation, we established that CD45.2$^+$*Cx3cr1*-GFP$^+$ SAMs repopulated sympathetic nerve bundles in WAT, whereas microglial repopulation in the brain did not occur (**Supplementary Fig. 4d**). This suggests that SAMs in sympathetic fibers have an origin similar to that of other hematopoietic macrophages rather than being from a microglial lineage.

SAM expression profile is more macrophage- than glial-like

Considering the association of SAMs with neurons, we asked how the gene expression profile of SAMs compared to those of other tissue-resident macrophages and microglia (**Fig. 2**). We sorted macrophages from various tissues as described above (F4/80$^+$CD45$^+$ cells designated as SAM ganglia, SAM fibers, sATMs, vATMs, SpMs, and microglia; **Fig. 2a** and **Supplementary Fig. 3**) and profiled gene expression by low-input RNA-seq (**Fig. 2b–f**). As expected, SAMs highly expressed markers common to both microglia and macrophages, such as *Adgre1*, *Csf1r*, and *Cx3cr1* (**Fig. 2b**). SAMs expressed macrophage-associated genes whose expression was excluded from microglia, such as *Fn1* and *Ciita* (**Fig. 2b**)[7]. Flow cytometric analysis showed that additional macrophage-specific markers whose expression was excluded from microglia (CD68, Ly6C, major histocompatibility complex II (MHCII), and CD11b) were also highly expressed in SAMs (**Supplementary Fig. 5a**,**b**). SAMs did not robustly express microglial- or glial-specific genes relative to macrophage-specific genes (**Fig. 2b** and **Supplementary Fig. 5c**)[8–17]. Expression of the *Sall1* gene, encoding a key microglial lineage-determining transcription factor, was strikingly absent from SAMs[18] (**Fig. 2b**).

Principal-component analysis (PCA) of the RNA-seq data showed tight clustering across replicates, indicating low contamination and high reproducibility (**Fig. 2d**). The absence of tyrosine hydroxylase (*Th*) expression in SAMs (**Supplementary Fig. 5d**) further excluded the possibility of contaminating cargo from neighboring cells, as *Th* was highly expressed in adjacent SNS neurons (**Fig. 1b**,**d**). PCA indicated that SAMs from fibers and ganglia were closely related, but both were distant from microglia and other macrophages (**Fig. 2d**). This was confirmed by phylogenetic analysis (**Fig. 2e**).

We hypothesized that the increased motility of SAMs (**Fig. 1c**) could indicate an activated, proinflammatory state. Therefore, we measured expression of a constellation of pro- and anti-inflammatory markers in SAMs by RNA-seq (**Fig. 2c**). Relative to other macrophage populations, SAMs highly expressed genes associated with macrophage activation, including *Cxcl2*, *Tnf*, *Socs3*, and *Il1a* (**Fig. 2c**), suggesting a constitutively proinflammatory steady state.

SAMs are phylogenetically distinct from other macrophages

Consistent with the PCA results (**Fig. 2d**), Pearson correlation analyses of transcript levels indicated differential expression patterns across SAMs, sATMs, vATMs, SpMs, and microglia (**Supplementary Fig. 6a**,**b**). Adipose tissue macrophages (sATMs and vATMs) showed similar expression landscapes ($R = 0.92$) that were distant from those of SAMs in fibers ($R = 0.63$ for sATMs and $R = 0.61$ for vATMs; **Supplementary Fig. 6b**). The expression landscapes of microglia and spleen macrophages were least correlated with other groups (**Supplementary Fig. 6b**).

Gene ontology analyses identified several biological processes associated with genes whose expression was enriched in SAMs relative to surrounding sATMs (**Supplementary Fig. 6c**). SAMs preferentially expressed genes involved in synaptic signaling, cell–cell adhesion, and neuron development (**Supplementary Fig. 6c**), suggesting that these cells fulfill an intrinsic role in local neuronal maintenance. Taken together, these data demonstrate divergent gene expression patterns in SAMs and ATMs, constituting within-tissue macrophage specialization.

SAMs import and degrade but do not synthesize NE

We next examined specific transcripts corresponding to the genes with divergent macrophage expression. The aforementioned populations of macrophages were sorted (**Fig. 2a** and **Supplementary Fig. 3**) for transcriptome analysis via low-input RNA-seq. Considering the gene ontology results (**Supplementary Fig. 6c**) and spatial proximity of SAMs to nerves (**Fig. 1**), we hypothesized that there would be differential expression of neurotransmitter receptors, transporters, or catalytic enzymes among these macrophage populations (**Fig. 2f**). In agreement with the Immunological Genome Project (ImmGen) database, we detected abundant expression of the *Adrb2* gene encoding β2 adrenergic receptor in all macrophage populations (**Fig. 2f**), which was confirmed by qRT–PCR (**Supplementary Fig. 6d**).

However, SAMs were the only population that expressed *Slc6a2*, the gene encoding the NE transporter (**Fig. 2f**). Similarly, *Maoa* was highly expressed in SAMs relative to the other macrophage types (**Fig. 2f**). Both results were validated by qRT–PCR (**Fig. 2g**,**h** and **Supplementary Table 1**). As SLC6A2 imports and MAOA degrades NE, we also tested for the presence of NE and detected it through enzyme-linked immunosorbent assay (ELISA) in sorted SAMs (**Fig. 2i** and **Supplementary Fig. 6e**). In agreement with our results, neither *Slc6a2* nor *Maoa* was substantially expressed in any macrophage population listed in the ImmGen database. Furthermore, we validated SLC6A2 and MAOA protein expression by immunofluorescence in SNS nerve fibers and SCG cryosections from *Cx3cr1*$^{GFP/+}$ mice (**Fig. 2j**,**k**). Representative photomicrographs show that GFP-expressing SAMs were double positive for membrane-bound SLC6A2 (**Fig. 2j**) and mitochondria-bound MAOA (**Fig. 2k**).

As SAMs, but not the other macrophage types assessed, possess the molecular machinery for import (**Fig. 2f**,**g**,**j**) and degradation (**Fig. 2f**,**h**,**k**) of NE, as well as considerably more NE than other macrophages (**Fig. 2i** and **Supplementary Fig. 6e**), we tested the possibility that SAMs synthesize NE. Through qRT–PCR of sorted SAMs, we did not detect expression of *Th*, which encodes an enzyme necessary for NE biosynthesis (**Supplementary Fig. 5d**). Taken together, these results indicate that SAMs have the molecular machinery for importing and degrading NE but not for biosynthesis of it.

To explore the responsiveness of SAMs to NE, we optogenetically stimulated sympathetic neurons in SCG cultures from mice produced by crossing *Th-cre* mice with *loxP*-STOP-*loxP* (LSL)-*ChR2-YFP* mice[1], which allowed us to visualize sympathetic neuron–macrophage interactions *ex vivo* (**Fig. 3a**,**b**). After optogenetic stimulation, we measured the NE content of sorted CD45$^+$F4/80$^+$ cells. SAMs from channelrhodopsin-2 (ChR2)$^+$ cultures exhibited significantly higher NE levels (**Fig. 3c**) that were proportional to NE availability in the culture medium (**Fig. 3d**). NE release by ChR2$^+$ neurons was significantly higher than that from ChR2$^-$ neurons (**Fig. 3d**). Uptake of NE by SAMs was prevented by pharmacological blockade of SLC6A2 using the pharmacological inhibitor nisoxetine, despite the significant increase of NE in the culture medium (**Fig. 3c**,**d**).

To validate our optogenetic findings with a physiologically relevant stimulus, we activated SNS explants with acetylcholine (ACh), which is presynaptically released from spinal cord neurons to innervate SCGs.

ACh-treated CD45$^+$F4/80$^+$ cells sorted from SCG explants contained significantly higher levels of NE than vehicle-treated controls (**Fig. 3e**). We validated that blockade of the NE importer SLC6A2 by nisoxetine prevented NE accumulation in SAMs (**Fig. 3e**). Co-incubation with ACh and nisoxetine further abolished NE uptake (**Fig. 3e**), despite the substantial increase in extracellular NE levels in the culture medium (**Fig. 3f**). These results, along with the negligible expression levels of *Chrna1* (*AChR*) in SAMs (**Supplementary Fig. 7a**; also validated by qRT–PCR in **Supplementary Fig. 7b**), exclude a role for acetylcholine receptors (AChRs) in mediating NE import.

Next, we assessed the effect of blocking MAOA on NE content in CD45$^+$F4/80$^+$ cells (**Fig. 3e**). Treatment with the MAOA inhibitor

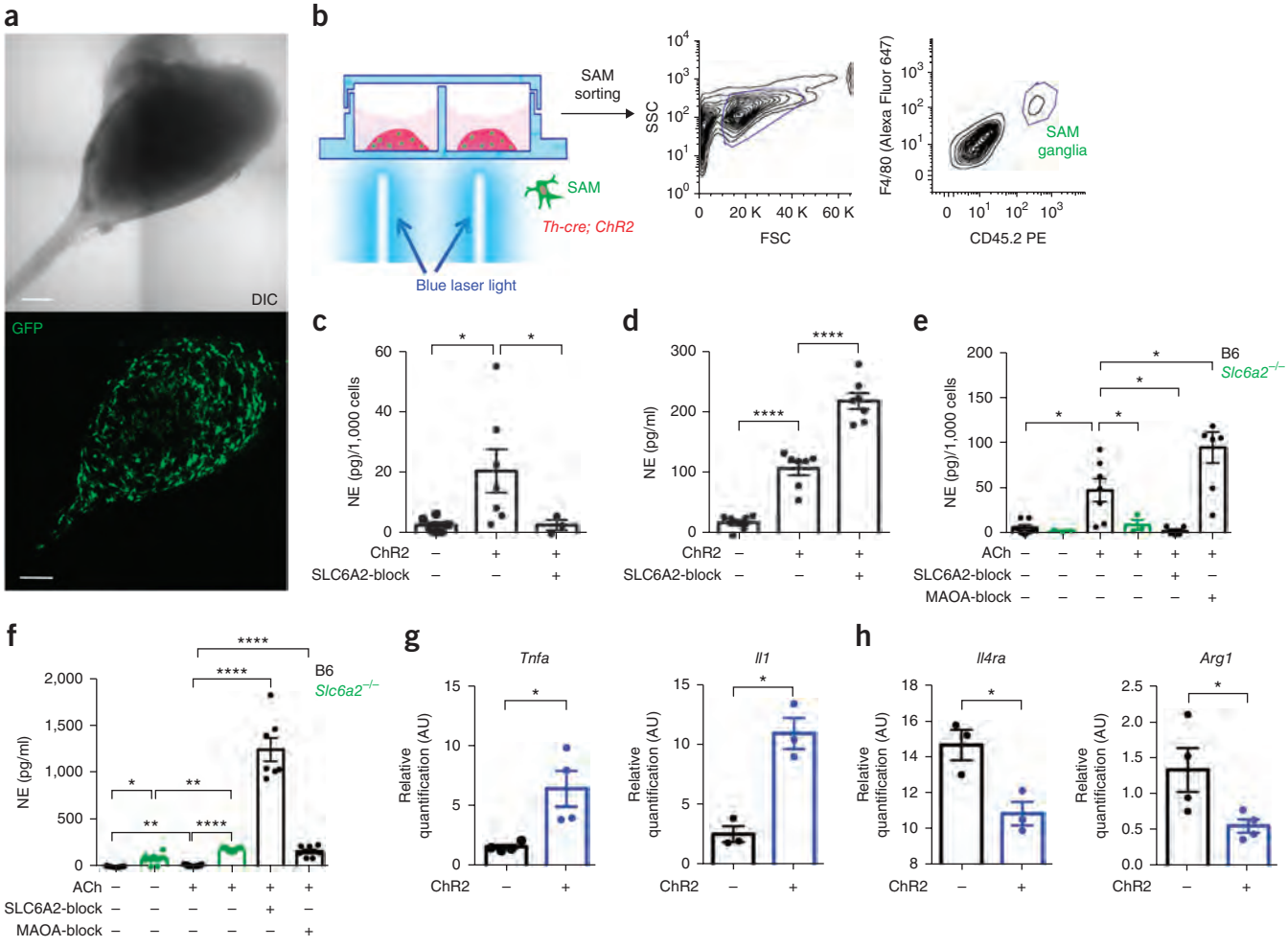

Figure 3 SAMs import and metabolize norepinephrine via SLC6A2 and MAOA, respectively, to regulate extracellular norepinephrine availability. (**a**) Representative images of *ex vivo* SCG explant cultures. Top, the area of the sympathetic ganglia is represented using the reflected-light differential interference contrast (DIC) channel. Bottom, *Cx3cr1*-GFP$^+$ cells in the same explant culture (GFP channel). Images are representative of 20 similar experiments. Scale bar, 100 µm. (**b**) Schematic representation of optogenetic activation of sympathetic SCG explant culture (left) followed by CD45.2 (PE)$^+$F4/80 (Alexa Fluor 647)$^+$ cell sorting (right). FSC, forward scatter; SSC, side scatter. (**c**) NE content in CD45.2$^+$F4/80$^+$ cells isolated from SCG explant cultures from *Th-cre*; LSL-*ChR2-YFP* and LSL-*ChR2-YFP* mice after optogenetic activation. Each data point represents tissues pooled from six mice. n = 3–7 experiments. The following numbers of cells were used in NE assays (run in duplicate): 189 ± 30 from *Th-cre*; LSL-*ChR2-YFP* SCG (n = 7), 126 ± 21 from LSL-*ChR2-YFP* SCG (n = 6), and 159 ± 19 from *Th-cre*; LSL-*ChR2-YFP* SCG stimulated with SLC6A2 blocker (n = 3). (**d**) *Ex vivo* NE release upon optogenetic stimulation of SCG explants isolated from *Th-cre*; LSL-*ChR2-YFP* and LSL-*ChR2-YFP* mice. Each data point represents medium collected from one explant culture. n = 7 per group. (**e**) NE content in CD45.2$^+$F4/80$^+$ cells isolated from the SCG of either B6 or *Slc6a2*$^{-/-}$ mice and then incubated with ACh, ACh and SLC6A2 blocker, ACh and MAOA blocker, or culture medium. Each data point represents tissues pooled from six mice. n = 3–7 experiments. The following numbers of cells were used in NE assays (run in duplicate): 364 ± 128 from B6 SCG (n = 7), 238 ± 55 from *Slc6a2*$^{-/-}$ SCG (n = 3), 216 ± 58 from B6 SCG incubated with ACh (n = 7), 201 ± 63 from *Slc6a2*$^{-/-}$ SCG incubated with ACh (n = 3), 196 ± 18 from B6 SCG incubated with ACh and SLC6A2 blocker (n = 5), and 133 ± 11 from B6 SCG incubated with ACh and MAOA blocker (n = 7). (**f**) *Ex vivo* NE release from the SCG of either B6 or *Slc6a2*$^{-/-}$ mice after incubation with ACh, ACh and SLC6A2 blocker, ACh and MAOA blocker, or culture medium. Each data point represents medium collected from one explant culture. n = 7 per group. (**g**) Expression of mRNA as determined by qRT–PCR relative to *Gapdh* expression for proinflammatory genes (*Tnfa* and *Il1*) in CD45.2$^+$F4/80$^+$ cells isolated from SCG explant cultures from *Th-cre*; LSL-*ChR2-YFP* (blue) and LSL-*ChR2-YFP* (black) mice. Prior to cell sorting, SCG explants were optogenetically stimulated. n = 3–4 experiments (for *Tnfa*, n = 4, P = 0.0467; for *Il1*, n = 3, P = 0.011). (**h**) Expression of mRNA as determined by qRT–PCR relative to *Gapdh* expression for anti-inflammatory genes (*Il4ra* and *Arg1*) in CD45.2$^+$F4/80$^+$ cells isolated from SCG explant cultures from *Th-cre*; LSL-*ChR2-YFP* (blue) and LSL-*ChR2-YFP* (black) mice. Prior to cell sorting, SCG explants were optogenetically stimulated. n = 3–4 experiments (for *Il4ra*, n = 3, P = 0.0257; for *Arg1*, n = 4, P = 0.0497). Data in **c**–**h** were analyzed by two-tailed unpaired Student's t-test and are shown as average ± s.e.m. *P < 0.05, **P < 0.01, ****P < 0.0001.

clorgyline was sufficient to nearly double intracellular NE levels in SAMs (**Fig. 3e**). In agreement with this finding, clorgyline increased NE levels in the medium (**Fig. 3f**), to which neuronal MAOA expression may also contribute. Genetic ablation of *Slc6a2* (in SCG cultures isolated from *Slc6a2*$^{-/-}$ mice) prevented NE uptake by SAMs regardless of NE availability in the culture medium (**Fig. 3e**,**f**). Finally, ATMs cultured *in vitro* with NE did not accumulate intracellular NE (**Supplementary Fig. 7c**), further demonstrating the specificity of NE uptake by SAMs. Altogether, our results indicate that *Slc6a2* is required for NE accumulation in SAMs.

We further probed whether the availability of NE, which can be manipulated *in vivo* by optogenetic activation of SNS neurons, changes the inflammatory profile of SAMs. We found that optogenetic stimulation of SCG explants correlated with an increase in proinflammatory gene expression, as measured by changes in expression of *Tnf* (*Tnfa*) and *Il1a* (*Il1*) (**Fig. 3g**), and a decrease in the expression of anti-inflammatory genes, as measured by changes in expression of *Il4r* (*Il4ra*) and *Arg1* (**Fig. 3h**).

SAMs are recruited and activated in obesity

We next used two mouse models to characterize the effect of obesity on tissue-specific functions of SAMs. In total, we employed four experimental groups: HFD, *Lep* (*Leptin*)-deficient (*ob*/*ob*), normal diet (ND), and 24-h-fasted ND mice. Flow cytometric analysis demonstrated that both obesity models (HFD and *ob*/*ob*) exhibited significantly higher percentages of SAMs than lean mice (ND) (**Fig. 4a** and **Supplementary Fig. 8a**). Furthermore, the acute metabolic challenge of fasting did not result in upregulation of SAMs, suggesting an obesity-specific causation of elevated macrophage content in sympathetic fibers (**Fig. 4a** and **Supplementary Fig. 8a**). Within the F4/80^{+}

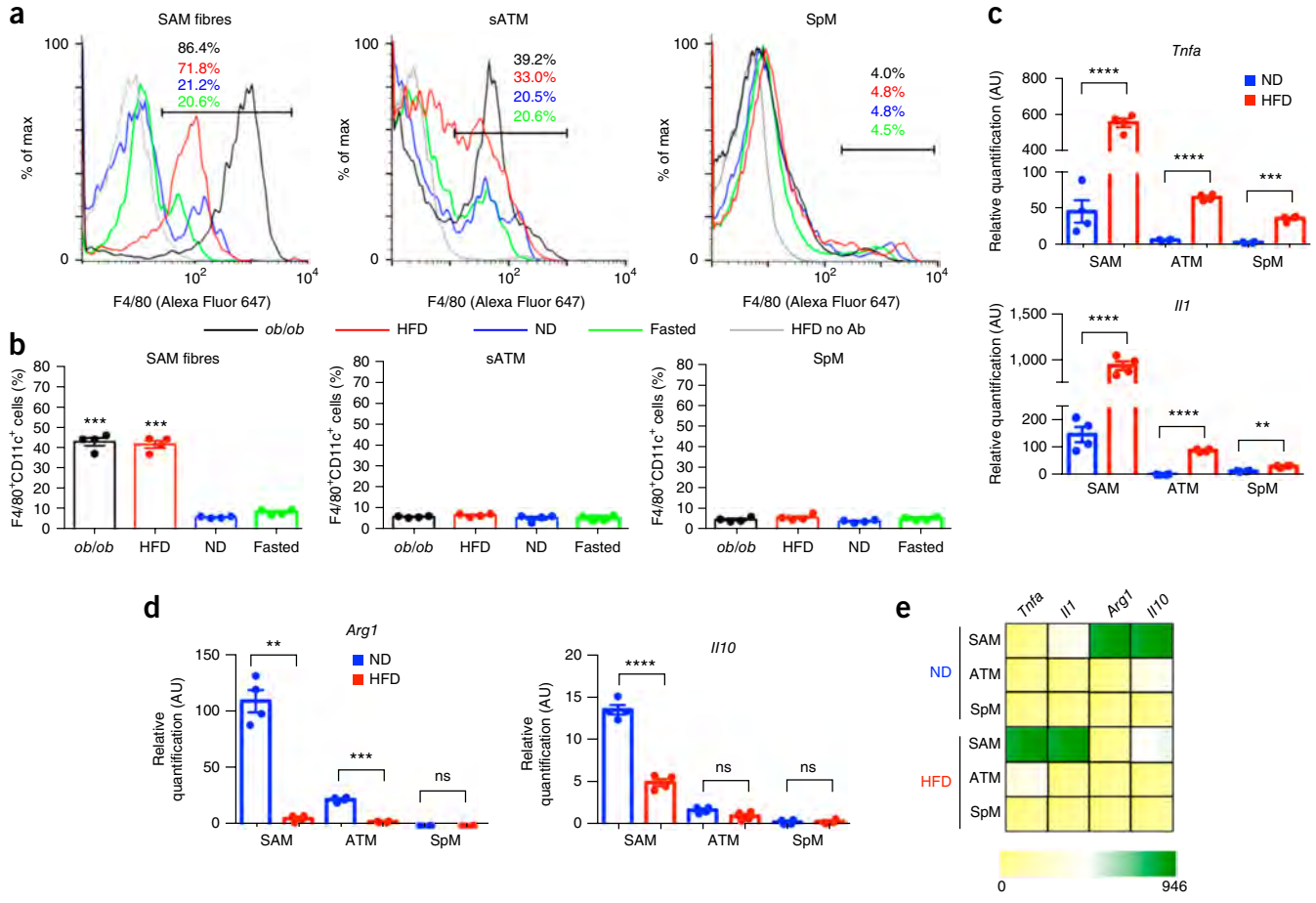

Figure 4 Obesity-induced accumulation of SAMs. (**a**) Representative histograms showing percentages of F4/80 (Alexa Fluor 647)$^{+}$ cells in sympathetic nerve fibers (left), subcutaneous adipose tissue (middle), and spleen (right) in mice that were genetically obese (*ob*/*ob*; black), obese due to HFD (red), ND fed (blue), or fasted for 24 h (green). CD45.2 (PE)$^{+}$ cells were gated. Histograms are representative of four independent experiments. HFD no Ab, cells without antibody staining harvested from mice fed a HFD. Black lines indicate the region defining F4/80^{+} cells. (**b**) Percentages of F4/80 (Alexa Fluor 647)$^{+}$CD11c (FITC)$^{+}$ cells in sympathetic nerve fibers (left), subcutaneous adipose tissue (middle), and spleen (right) in mice that were genetically obese (*ob*/*ob*; black), obese due to HFD (red), ND fed (blue), or fasted for 24 h (green). CD45.2 (PE)$^{+}$ cells were gated. $n = 4$ experiments per group. Each data point represents one experiment. (**c**) Expression of mRNA as determined by qRT–PCR relative to *Gapdh* expression for proinflammatory genes (*Tnfa* and *Il1*) in CD45.2^{+}F4/80^{+} cells in sympathetic nerve fibers (SAMs), subcutaneous adipose tissue (ATMs), and spleen (SpMs) isolated from mice that were fed either ND (blue) or HFD (red). $n = 4$ experiments per group. Each data point represents tissues pooled from ten mice. (**d**) Expression of mRNA as determined by qRT–PCR relative to *Gapdh* expression for anti-inflammatory genes (*Arg1* and *Il10*) in CD45.2^{+}F4/80^{+} cells including SAMs, ATMs, and SpMs isolated from mice that were fed either ND (blue) or HFD (red). $n = 4$ experiments per group. Each data point represents tissues pooled from ten mice. (**e**) Heat map showing the expression of pro- and anti-inflammatory genes as determined by the qRT–PCR analyses in **c** and **d**. Data in **b** were analyzed by one-way ANOVA followed by Bonferroni multiple-comparisons test with ND as the control group. Data in **c** and **d** were analyzed by two-tailed unpaired Student's *t*-test. Data are shown as average ± s.e.m. $^{**}P < 0.01$, $^{***}P < 0.001$, $^{****}P < 0.0001$; ns, not significant.

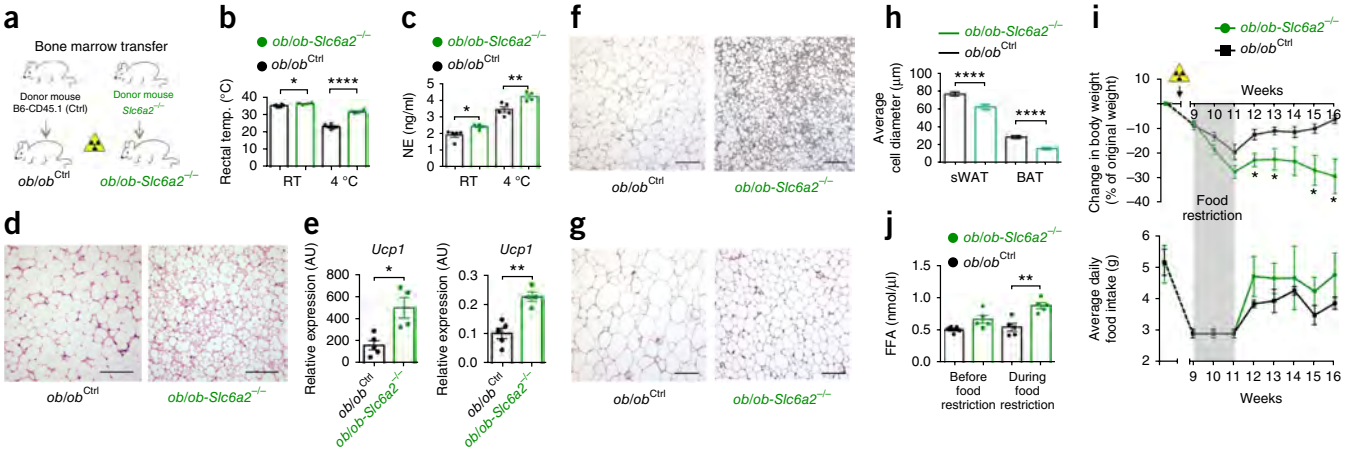

Figure 5 Loss of *Slc6a2* function in SAMs rescues the thermogenic capacity of *ob*/*ob* mice. (**a**) Schematic representation of bone marrow transplant from either *Slc6a2*$^{-/-}$ or control B6 (CD45.1) mice into genetically obese *ob*/*ob* mice (*ob*/*ob-Slc6a2*$^{-/-}$ and *ob*/*ob*^{Ctrl} chimeras, respectively). (**b**) Rectal temperature of *ob*/*ob*^{Ctrl} (black) and *ob*/*ob-Slc6a2*$^{-/-}$ (green) chimeras was measured at room temperature (RT) and after 2 h of cold challenge (4 °C). Each data point represents one mouse. $n = 4$ *ob*/*ob-Slc6a2*$^{-/-}$ mice and $n = 6$ *ob*/*ob*^{Ctrl} mice. $^{*}P = 0.025$, $^{****}P < 0.0001$. (**c**) Serum levels of NE in *ob*/*ob*^{Ctrl} (black) and *ob*/*ob-Slc6a2*$^{-/-}$ (green) chimeras were measured at room temperature and after 2 h of cold exposure (4 °C). Each data point represents one mouse. $n = 4$ mice per group for *ob*/*ob-Slc6a2*$^{-/-}$ mice and $n = 5$ mice per group for *ob*/*ob*^{Ctrl} mice. $^{*}P = 0.022$, $^{**}P = 0.0072$. (**d**) Optical micrographs of BAT removed from *ob*/*ob* chimeras following 2 h of cold challenge (4 °C) and stained with H&E. Left, BAT from an *ob*/*ob*^{Ctrl} chimera. Right, BAT from an *ob*/*ob-Slc6a2*$^{-/-}$ chimera. Images are representative of fat organs collected from four *ob*/*ob*^{Ctrl} and six *ob*/*ob-Slc6a2*$^{-/-}$ mice. (**e**) Expression of mRNA for *Ucp1* as determined by qRT–PCR relative to *Gapdh* expression in BAT (left) and sWAT (right) dissected after 2 h of cold challenge (4 °C). Each data point represents one mouse. $n = 4$ *ob*/*ob-Slc6a2*$^{-/-}$ mice (green) and $n = 5$ *ob*/*ob*^{Ctrl} mice (black). $^{*}P = 0.0269$, $^{**}P = 0.0015$. (**f**) Optical micrographs of BAT dissected from *ob*/*ob*^{Ctrl} (left) and *ob*/*ob-Slc6a2*$^{-/-}$ (right) chimeras following 2 h of cold challenge (4 °C) and stained with anti-UCP1 antibody. Images are representative of fat organs collected from four *ob*/*ob*^{Ctrl} and six *ob*/*ob-Slc6a2*$^{-/-}$ mice. (**g**) Optical micrographs of sWAT dissected from *ob*/*ob*^{Ctrl} (left) and *ob*/*ob-Slc6a2*$^{-/-}$ mice (right) following 2 h of cold challenge (4 °C) and stained with anti-UCP1 antibody. Images are representative of fat organs collected from four *ob*/*ob*^{Ctrl} and six *ob*/*ob-Slc6a2*$^{-/-}$ mice. (**h**) Average adipocyte diameter quantified from optical micrographs of sWAT and BAT from *ob*/*ob* chimeras following 2 h of cold challenge (4 °C). Measurements are representative of four (*ob*/*ob-Slc6a2*$^{-/-}$) and six (six *ob*/*ob*^{Ctrl}) independent micrographs. 18–34 measurements were obtained per micrograph. $n = 169$ cells for *ob*/*ob*^{Ctrl} sWAT, $n = 120$ cells for *ob*/*ob-Slc6a2*$^{-/-}$ sWAT, $n = 180$ cells for *ob*/*ob*^{Ctrl} BAT, $n = 120$ cells for *ob*/*ob-Slc6a2*$^{-/-}$ BAT. $^{****}P < 0.0001$. (**i**) Body weight change (top) and daily food intake (bottom) of *ob*/*ob*^{Ctrl} ($n = 4$ mice) and *ob*/*ob-Slc6a2*$^{-/-}$ ($n = 6$ mice) chimeras monitored for 7 weeks following 2 weeks of food intake normalization (0.06 g of food per 1 g of body weight per day; gray shading) that started 9 weeks after bone marrow transplant. The yellow triangle indicates when irradiation was performed. $^{*}P < 0.05$. (**j**) Blood plasma nonesterified (free) fatty acid (FFA) concentration in *ob*/*ob*^{Ctrl} and *ob*/*ob-Slc6a2*$^{-/-}$ chimeras measured 8 weeks after bone marrow transplant before and while mice were under a regimen of 0.06 g of food per 1 g of body weight per day. $n = 5$ mice per group. $^{**}P = 0.0022$. Data in **b**, **c**, **e**, **h**, and **j** were analyzed by two-tailed unpaired Student's *t*-test and in **i** by multiple *t*-tests (one Student's *t*-test per row with correction for multiple comparisons using the Holm–Sidak method). Data are shown as average ± s.e.m. Scale bars in **d**, **f**, and **g**, 100 µm.

SAM fraction from HFD and *ob*/*ob* mice, we noted a high frequency of CD11c^{+} cells (**Fig. 4b**), which are hallmarks of inflammation and insulin resistance in human obesity[19]. In contrast to SAM accumulation in SNS nerve fibers dissected from WAT, SAMs did not accumulate in SCG, which innervates neck structures such as salivary glands (**Supplementary Fig. 8b**).

The differential distribution of macrophages under conditions of obesity suggests that cytokine levels are also sensitive to obesity. Comparison of the anti- and proinflammatory gene profiles of SAMs, ATMs, and SpMs (**Fig. 4c–e**) revealed that obesity correlated with higher levels of proinflammatory genes (i.e., *Tnfa* or *Il1*; **Fig. 4c**,**e**) and lower levels of anti-inflammatory genes (i.e., *Arg1* or *Il10*; **Fig. 4d**,**e**).

To determine whether local proliferation contributes to SAM accumulation, we measured the proliferation marker Ki-67 in SAMs by flow cytometry (**Supplementary Fig. 8c**,**d**). We observed that obesity (in the HFD and *ob*/*ob* models) did not substantially increase Ki-67^{+} SAM percentage, whereas (in accordance with previous reports[20]) obesity increased Ki-67^{+} ATMs from sWAT (**Supplementary Fig. 8d**).

Slc6a2 deletion in SAMs rescues obesity

We probed how ablating *Slc6a2* in SAMs affects obesity-associated pathology. We considered a Cre–*loxP* approach, but the established macrophage Cre lines (*Cx3cr1-cre*[21,22] and *LyzM-cre*[23]) would not allow for specificity of ablation to SAMs. We thus took advantage of the cell-type specificity of *Slc6a2* expression, which is high in SAMs but negligible in other macrophage and hematopoietic cell populations (**Fig. 2b**,**g** and ImmGen[24]). We validated that there was not another population of hematopoietic origin expressing *Slc6a2* aside from SAMs; a rare population of CD45^{+}F4/80^{-} cells was present in SCG (**Supplementary Fig. 9a**) but did not express SLC6A2 (**Supplementary Fig. 9b**). SAM-specific genetic ablation of *Slc6a2* was achieved through bone marrow transfer from *Slc6a2*$^{-/-}$ mice[25] into genetically obese *ob*/*ob* recipients (*ob*/*ob-Slc6a2*$^{-/-}$; **Fig. 5a**). Control chimeras consisted of *ob*/*ob* mice (*ob*/*ob*^{Ctrl}) that received a bone marrow transfer from B6 CD45.1 mice. Chimeras recovered for 9 weeks following transplant to allow irradiation-induced inflammation to subside.

As cold temperature is a robust driver of SNS activity, we challenged mice for 2 h at 4 °C and observed that *ob*/*ob-Slc6a2*$^{-/-}$ chimeras displayed superior capacity for maintaining body temperature as compared to control *ob*/*ob*^{Ctrl} chimeras (**Fig. 5b**). These thermogenic effects were accompanied by significant upregulation of NE levels in serum (**Fig. 5c**), rescue of BAT morphology (**Fig. 5d**), and browning of white fat, as measured by *Ucp1* mRNA and uncoupling protein 1 (UCP1) levels (**Fig. 5e–g**).

Transplant of bone marrow from *Slc6a2*$^{-/-}$ mice into *ob*/*ob* mice prevented obesity-induced hypertrophy of both BAT and WAT adipocytes (**Fig. 5h**) but did not affect total body weight (**Fig. 5i**). Because food-restriction challenge drives SNS activity and mobilizes lipid stores from adipose tissue, we normalized the daily food intake of the *ob*/*ob* chimeras for 2 weeks (**Fig. 5i**,**j**). After a dieting challenge, *ob*/*ob*-*Slc6a2*$^{-/-}$ mice lost nearly 30% of their body weight relative to their original body weight, after which their body weight was stable for up to 16 weeks, even after they were given *ad libitum* access to food (**Fig. 5i**). We also found that *ob*/*ob*-*Slc6a2*$^{-/-}$ mice exhibited higher lipid mobilization during food restriction relative to controls (**Fig. 5j**).

We analyzed wild-type B6 chimeras reconstituted with bone marrow from *Slc6a2*$^{-/-}$ mice relative to CD45.1 controls (B6-*Slc6a2*$^{-/-}$ and B6^{Ctrl} chimeras, respectively) (**Supplementary Fig. 9c**). SAMs from B6-*Slc6a2*$^{-/-}$ chimeras did not accumulate NE (**Supplementary Fig. 9d**). In accordance with the results from *ob*/*ob* chimeras (**Fig. 5**), B6-*Slc6a2*$^{-/-}$ chimeras also exhibited increased serum levels of NE, thermogenesis, and lipolysis, as well as marked weight loss, relative to control mice (**Supplementary Fig. 9e**–**i**). Upon challenge with HFD, we observed weight-gain prevention in B6-*Slc6a2*$^{-/-}$ but not B6^{Ctrl} mice (**Supplementary Fig. 9g**). These results indicate a notable anti-obesity effect of SAM-specific *Slc6a2* ablation.

SAMs are in BAT and act as a NE sink

In light of the enhanced thermogenic capacity of *ob*/*ob*-*Slc6a2*$^{-/-}$ chimeras, we questioned whether SAMs are present in BAT (**Supplementary Fig. 10**). BAT did contain *Cx3cr1*-GFP^{+} cells (in accordance with a previous report[19]) that exhibited a morphology intermediate to those of SAMs (multiple pseudopodia) and ATMs (round) (**Supplementary Fig. 10a** as compared to **Fig. 1c**). Some of these cells appeared to make close contacts with thin TH^{+} axons (**Supplementary Fig. 10a**). Because TH^{+} nerve fibers in BAT are too delicate for dissection, we sorted macrophages from whole BAT for qRT–PCR analysis. *Slc6a2* and *Maoa* were expressed in BAT macrophages, although at lower levels than in SAMs isolated from dissected SNS nerve bundles in sWAT or SCG (**Supplementary Fig. 10b**,**c**). We also detected the presence of NE in BAT macrophages, although at lower levels than SAMs (**Supplementary Fig. 10d**). The lower levels of *Slc6a2*, *Maoa*, and NE content may reflect a dilution of BAT SAMs by BAT ATMs, as mixed (as opposed to isolated) populations were analyzed.

Finally, we used *LyzM-cre*; *Csf1r*-LSL-*DTR* mice with conditional expression of diphtheria toxin receptor (DTR) on macrophages to test whether macrophages serve as a sink for NE. After validating ablation of macrophages (**Supplementary Fig. 11a**,**b**), we observed a significant increase of NE in sWAT of *LyzM-cre*; *Csf1r*-LSL-*DTR* mice relative to *Csf1r*-LSL-*DTR* controls (**Supplementary Fig. 11c**). Note that, owing to constant hematopoietic input, it is practically impossible to completely deplete macrophages. This limitation notwithstanding, these results are consistent with a model in which macrophages act as a sink for NE.

Human sympathetic ganglia also contain NE-degrading SAMs

Finally, we asked whether SAMs exist in humans. We obtained nine human excisional biopsies of SNS or thoracolumbar ganglia that were collected during sympathectomy and/or gangliotomy. We stained tissue sections with H&E (**Fig. 6a**,**b**) or an antibody against CD68, a human macrophage marker, and identified the presence of macrophages in SNS tissues (**Fig. 6c**,**d** and **Supplementary Fig. 12**).

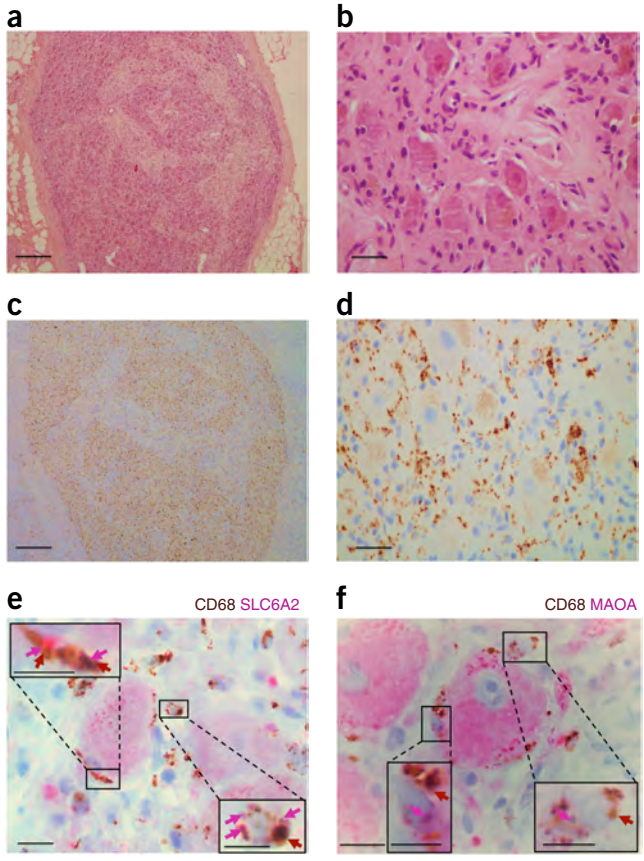

Figure 6 SAMs in the human sympathetic nervous system. (**a**,**b**) Optical micrograph of human ganglia from the thoracolumbar region stained with H&E (**a**) and a higher-magnification image (**b**). (**c**,**d**) Optical micrograph of human ganglia from the thoracolumbar region stained with an antibody against CD68 (**c**) and a higher-magnification image (**d**). (**e**) Optical micrograph of human ganglia from the thoracolumbar region stained with antibodies against CD68 and SLC6A2. Red arrows indicate CD68^{+}SLC6A2^{+} regions. Pink arrows indicate SLC6A2^{+} regions. (**f**) Optical micrographs of human ganglia from the thoracolumbar region stained with antibodies against CD68 and MAOA. Red arrows indicate CD68^{+}MAOA^{+} regions. Pink arrows indicate MAOA^{+} regions. Boxed regions in **e** and **f** represent higher-magnification images of the main micrographs. Scale bars: 1 mm (**a**,**c**), 100 µm (**b**,**d**), and 50 µm (**e**,**f**); for boxed regions, 25 µm. Images in **a**–**f** are representative of nine different human samples.

We next determined whether SAMs in human sympathetic ganglia also contain the machinery for uptake and degradation of NE (**Fig. 6e**,**f** and **Supplementary Fig. 12**). The CD68 macrophage marker colocalized with staining for SLC6A2 (**Fig. 6e** and **Supplementary Fig. 12a**) and MAOA (**Fig. 6f** and **Supplementary Fig. 12b**). Both SLC6A2^{+} and MAOA^{+} neurons existed, but the background levels were low relative to control human gut-associated lymphoid tissue (GALT) samples that also contained CD68^{+} macrophages (**Supplementary Fig. 12c**,**d**).

DISCUSSION

SAMs are a previously undescribed population of SNS-resident macrophages that import and degrade NE. To fulfill their function, SAMs express a dedicated molecular machinery that is, as best we can tell, absent from neighboring macrophages and other known macrophage populations (shown by our data and the ImmGen database). In SAMs, NE is imported by SLC6A2 and degraded by MAOA. This is a specialized

molecular mechanism for NE uptake with a role that is not fulfilled by the canonical phagocytic mechanisms generally present in macrophages[26].

Unlike most other neurons, which exclusively release neurotransmitter at a terminal synapse, SNS neurons also release NE via varicosities distributed along axons that can extend for tens of centimeters[27]. SAMs possibly serve to prevent NE spillover into the bloodstream or neighboring tissues when SNS activity is high. Indeed, we demonstrate that, when SNS neurons are optogenetically activated, SAMs import increased levels of NE and become more polarized toward a proinflammatory phenotype. In this regard, NE can be considered a noxious stimulus that must be locally delivered in a controlled manner to a target tissue. Chronic and excessive systemic NE in serum, such as the levels present under chronic stress conditions or in medullary adrenal tumors, leads to hypertension and cardiopathy due to direct action in cardiovascular tissues[28].

The activated polarization state of SAMs is consistent with a model in which these cells play a tissue-protective role by acting as a sentinel and scavenger of surplus levels of an endogenous neurotransmitter (i.e., NE) that, if released in excess from varicosities, could potentially be harmful. Tissue-protective immune cells have been documented in the brain and other, non-neuronal systems[29–34]. For instance, muscularis-resident macrophages in the gut induce rapid tissue-protective responses to potentially pathogenic insults via β2 adrenergic receptor signaling[35]. This mechanism and our study indicate specialization of macrophage populations for fulfillment of tissue-specific tasks in response to neuronal cues. Divergent gene expression landscapes across populations of resident macrophages isolated from different tissues support the idea of local macrophage adaptations[22,36,37]. In this study, we use transcriptional data to molecularly characterize SAMs alongside other macrophage populations. Our results suggest that macrophages associated with the SNS have specialized molecular programs, whose exploration might give further insight into mechanisms underlying SNS macrophage–neuron communication.

Although SAMs express common microglial genes and reside in proximity to nerve cells, SAM pseudopodia are morphologically distinct from the finely branching ramifications of resting microglia[38,39]. Moreover, SAMs are seemingly of hematopoietic origin, as suggested by our bone marrow chimera studies and their high expression of CD45 and macrophage markers. Future tracing studies are necessary to definitively determine SAM origin. To our knowledge, no reports exist on NE uptake by microglia, and we verified that the machinery for NE uptake is not expressed in these cells. In this regard, only one study has reported that NE can trigger microglia to import and degrade amyloid but not NE itself[40]. Neurotransmitter uptake has primarily been studied in astroglia, which are CX3CR1$^-$ (ref. 41).

Chimeric models require irradiation that generates inflammation. However, if given adequate recovery time (8 weeks), recruited macrophages dissipate from the brain, as represented in our chimeras by minimal residual *Cx3cr1*-GFP$^+$ microglia (0.06%). SAMs persist at levels that greatly surpass background irradiation-induced macrophage recruitment, and regenerated SAMs are seemingly identical to those in non-irradiated mice.

We show low expression of several astroglial markers in SAMs, raising the possibility of a hybrid peripheral cell type that unites some of the features of macrophages and glia. Alternatively, genes expressed in common by glial cells and SAMs may be attributable to the proximity of SAMs to neuron-derived signals, analogous to the observation that microglia, astrocytes, and neurons share the expression of certain central nervous system–specific genes[7,42]. An alternative model is that SAMs share the lineage of satellite glial cells (SGCs), which are derived from embryonic neural crest[11] and also express canonical astroglial markers[43]. However, SGC import or degradation of NE has not been reported[44].

Our study may fill a gap in the literature by demonstrating a cellular and molecular mechanism alternative to the proposed existence of NE-producing macrophages in WAT[3]. In this regard, our findings are consistent with other reports[4–6], as we did not detect the NE biosynthetic machinery in SAMs nor in ATMs. The identification of SAMs sheds new light on this recent controversy by documenting how a particular population of macrophages can contain NE in the absence of its biosynthesis. We also document that BAT macrophages contain similar molecular machinery to that in SAMs for NE uptake, extending and validating the findings of our colleagues[21]. SAMs may play a tissue-protective role through regulation of regional NE levels by serving as a local sink that prevents the dangerous effects of chronically increased levels of systemic NE.

In sharp contrast to the anti-inflammatory state of intestinal nerve–associated *Cx3cr1*-GFP$^+$ macrophages[35], SAMs exhibit a proinflammatory profile at steady state. This could be due to the constitutive presence of a danger signal—namely, NE. Whether this polarization is caused by NE import or by adrenergic signaling remains to be established. In this regard, polarization of enteric-associated macrophages has been linked to activation of β2 adrenergic receptor, which is also expressed in SAMs[35]. Regardless, our core message is relevant: SAMs are proinflammatory and act as a NE sink, and blocking NE uptake has an antiobesity effect. Our results support a model whereby SAMs pathologically accumulate in the SNS nerves of obese subjects in an organ-specific manner, thus explaining why we detect SAM accumulation in the WAT-associated SNS but not in SCG, which innervates salivary glands and other neck structures. The NE-scavenging role of SAMs may have become evolutionarily maladaptive, as in the past obesity was not a common physiological stress to which humans had to adapt. In modern times, the prevalence of overnutrition has created a need for increased lipolysis-inducing NE signaling to maintain fat stores, which is obstructed by the 'original' function of SAMs to limit NE levels.

Reduced NE availability in the adipose tissue is linked to blunted lipolysis and obesity. Very recently, our colleagues have shown that ATMs degrade NE during aging[45]. Whether this observation is also associated with the accumulation of SAMs in fat, as we observed in the two mouse models of obesity, remains to be established.

Our results demonstrate that SAM-specific *Slc6a2* ablation rescues BAT and adaptive thermogenesis in obese *ob*/*ob* mice, which in turn leads to sustained weight loss and lipid mobilization. We determine that blocking NE import into SAMs mitigates the recidivism of obesity that is typical after dieting. Overall, our results identify SAMs as a potential new molecular and cellular target for obesity therapy.

METHODS

Methods, including statements of data availability and any associated accession codes and references, are available in the online version of the paper.

Note: Any Supplementary Information and Source Data files are available in the online version of the paper.

ACKNOWLEDGMENTS

We would like to thank the Unit for Imaging and Cytometry at the Instituto Gulbenkian de Ciência (IGC) for assistance with flow cytometry, cell sorting, and multiphoton microscopy. We also want to thank the Antibody Service at the IGC

for the antibodies produced in house and the Histopathology facility at the IGC for tissue processing and histological assessment. This work was supported by the Fundação para a Ciência e Tecnologia (FCT), the European Molecular Biology Organization (EMBO), the Human Frontier Science Program (HFSP), Maratona da Saúde, and the US National Institutes of Health (NIH). R.M.P. was supported by FCT (SFRH/BD/88454/2012), J.S.S. was supported by the American Heart Association (16PRE30980030) and a training grant (T32DK007541), B.A.A. was supported by Conselho Nacional de Desenvolvimento Científico e Tecnológico (CNPq), and N.M.-S. was supported by Xunta de Galicia (ED481B 2016/168-0). We thank M. Aouadi for helpful discussions.

AUTHOR CONTRIBUTIONS

A.I.D. conceptualized the study. R.M.P. performed two-photon and confocal microscopy. E.S. and R.M.P. performed flow cytometry. J.S.S. and R.M.P. performed low-input RNA-seq. V.M.L., J.S.S., and R.M.P. analyzed the RNA-seq data. M.I., A.L.S., S.A., and E.T. performed electron microscopy. E.S., R.M.P., N.M.S., I. Mahú, B.A.A., and C.M.L. performed functional tests. N.K., I. Morris, R.M., and V.G. performed related mouse husbandry and genotyping. F.T. and M.V. processed human ganglia. M.K.H. provided the *Slc6a2*$^{-/-}$ mice. N.J.S. developed the low-input RNA-seq protocols. A.I.D., C.K.G., and R.M.P. wrote the original draft of the manuscript. A.I.D., C.K.G., R.M.P., and C.M.L. reviewed and edited the final version of the manuscript.

COMPETING FINANCIAL INTRESTS

The authors declare no competing financial interests.

1. Zeng, W. *et al.* Sympathetic neuro-adipose connections mediate leptin-driven lipolysis. *Cell* **163**, 84–94 (2015).
2. Mathis, D. Immunological goings-on in visceral adipose tissue. *Cell Metab.* **17**, 851–859 (2013).
3. Nguyen, K.D. *et al.* Alternatively activated macrophages produce catecholamines to sustain adaptive thermogenesis. *Nature* **480**, 104–108 (2011).
4. Fischer, K. *et al.* Alternatively activated macrophages do not synthesize catecholamines or contribute to adipose tissue adaptive thermogenesis. *Nat. Med.* **23**, 623–630 (2017).
5. Spadaro, O. *et al.* IGF1 shapes macrophage activation in response to immunometabolic challenge. *Cell Rep.* **19**, 225–234 (2017).
6. Reitman, M.L. How does fat transition from white to beige? *Cell Metab.* **26**, 14–16 (2017).
7. Gosselin, D. *et al.* Environment drives selection and function of enhancers controlling tissue-specific macrophage identities. *Cell* **159**, 1327–1340 (2014).
8. Anlauf, E. & Derouiche, A. Glutamine synthetase as an astrocytic marker: its cell type and vesicle localization. *Front. Endocrinol. (Lausanne)* **4**, 144 (2013).
9. Bignami, A., Eng, L.F., Dahl, D. & Uyeda, C.T. Localization of the glial fibrillary acidic protein in astrocytes by immunofluorescence. *Brain Res.* **43**, 429–435 (1972).
10. Chaudhry, F.A. *et al.* Glutamate transporters in glial plasma membranes: highly differentiated localizations revealed by quantitative ultrastructural immunocytochemistry. *Neuron* **15**, 711–720 (1995).
11. Jessen, K.R. & Mirsky, R. The origin and development of glial cells in peripheral nerves. *Nat. Rev. Neurosci.* **6**, 671–682 (2005).
12. Ludwin, S.K., Kosek, J.C. & Eng, L.F. The topographical distribution of S-100 and GFA proteins in the adult rat brain: an immunohistochemical study using horseradish peroxidase–labelled antibodies. *J. Comp. Neurol.* **165**, 197–207 (1976).
13. Mearow, K.M., Mill, J.F. & Vitkovic, L. The ontogeny and localization of glutamine synthetase gene expression in rat brain. *Brain Res. Mol. Brain Res.* **6**, 223–232 (1989).
14. Raff, M.C. *et al.* Galactocerebroside is a specific cell-surface antigenic marker for oligodendrocytes in culture. *Nature* **274**, 813–816 (1978).
15. Regan, M.R. *et al.* Variations in promoter activity reveal a differential expression and physiology of glutamate transporters by glia in the developing and mature CNS. *J. Neurosci.* **27**, 6607–6619 (2007).
16. Rusnakova, V. *et al.* Heterogeneity of astrocytes: from development to injury—single cell gene expression. *PLoS One* **8**, e69734 (2013).
17. Sensenbrenner, M., Lucas, M. & Deloulme, J.C. Expression of two neuronal markers, growth-associated protein 43 and neuron-specific enolase, in rat glial cells. *J. Mol. Med. (Berl.)* **75**, 653–663 (1997).
18. Buttgereit, A. *et al.* Sall1 is a transcriptional regulator defining microglia identity and function. *Nat. Immunol.* **17**, 1397–1406 (2016).
19. Wentworth, J.M. *et al.* Pro-inflammatory CD11c^{+}CD206^{+} adipose tissue macrophages are associated with insulin resistance in human obesity. *Diabetes* **59**, 1648–1656 (2010).
20. Amano, S.U. *et al.* Local proliferation of macrophages contributes to obesity-associated adipose tissue inflammation. *Cell Metab.* **19**, 162–171 (2014).
21. Wolf, Y. *et al.* Brown-adipose-tissue macrophages control tissue innervation and homeostatic energy expenditure. *Nat. Immunol.* **18**, 665–674 (2017).
22. Gosselin, D. *et al.* An environment-dependent transcriptional network specifies human microglia identity. *Science* **356**, eaal3222 (2017).
23. Clausen, B.E., Burkhardt, C., Reith, W., Renkawitz, R. & Förster, I. Conditional gene targeting in macrophages and granulocytes using LysMcre mice. *Transgenic Res.* **8**, 265–277 (1999).
24. Merad, M. *et al.* Langerhans cells renew in the skin throughout life under steady-state conditions. *Nat. Immunol.* **3**, 1135–1141 (2002).
25. Shirey-Rice, J.K. *et al.* Norepinephrine transporter variant A457P knock-in mice display key features of human postural orthostatic tachycardia syndrome. *Dis. Model. Mech.* **6**, 1001–1011 (2013).
26. Aderem, A. & Underhill, D.M. Mechanisms of phagocytosis in macrophages. *Annu. Rev. Immunol.* **17**, 593–623 (1999).
27. Stjärne, L. Basic mechanisms and local modulation of nerve impulse–induced secretion of neurotransmitters from individual sympathetic nerve varicosities. *Rev. Physiol. Biochem. Pharmacol.* **112**, 1–137 (1989).
28. Schroeder, C. & Jordan, J. Norepinephrine transporter function and human cardiovascular disease. *Am. J. Physiol. Heart Circ. Physiol.* **303**, H1273–H1282 (2012).
29. Filiano, A.J. *et al.* Unexpected role of interferon-γ in regulating neuronal connectivity and social behaviour. *Nature* **535**, 425–429 (2016).
30. Galle-Treger, L. *et al.* Nicotinic acetylcholine receptor agonist attenuates ILC2-dependent airway hyperreactivity. *Nat. Commun.* **7**, 13202 (2016).
31. Ibiza, S. *et al.* Glial-cell-derived neuroregulators control type 3 innate lymphoid cells and gut defence. *Nature* **535**, 440–443 (2016).
32. Kipnis, J. Multifaceted interactions between adaptive immunity and the central nervous system. *Science* **353**, 766–771 (2016).
33. Louveau, A. *et al.* Structural and functional features of central nervous system lymphatic vessels. *Nature* **523**, 337–341 (2015).
34. Rosas-Ballina, M. *et al.* Acetylcholine-synthesizing T cells relay neural signals in a vagus nerve circuit. *Science* **334**, 98–101 (2011).
35. Gabanyi, I. *et al.* Neuro-immune interactions drive tissue programming in intestinal macrophages. *Cell* **164**, 378–391 (2016).
36. Gautier, E.L. *et al.* Gene-expression profiles and transcriptional regulatory pathways that underlie the identity and diversity of mouse tissue macrophages. *Nat. Immunol.* **13**, 1118–1128 (2012).
37. Okabe, Y. & Medzhitov, R. Tissue-specific signals control reversible program of localization and functional polarization of macrophages. *Cell* **157**, 832–844 (2014).
38. Crotti, A. & Ransohoff, R.M. Microglial physiology and pathophysiology: insights from genome-wide transcriptional profiling. *Immunity* **44**, 505–515 (2016).
39. Prinz, M. & Priller, J. Microglia and brain macrophages in the molecular age: from origin to neuropsychiatric disease. *Nat. Rev. Neurosci.* **15**, 300–312 (2014).
40. Kong, Y., Ruan, L., Qian, L., Liu, X. & Le, Y. Norepinephrine promotes microglia to uptake and degrade amyloid β peptide through upregulation of mouse formyl peptide receptor 2 and induction of insulin-degrading enzyme. *J. Neurosci.* **30**, 11848–11857 (2010).
41. Kettenmann, H. & Ransom, B.R. *Neuroglia* (Oxford University Press, 2013).
42. Butovsky, O. *et al.* Identification of a unique TGF-β-dependent molecular and functional signature in microglia. *Nat. Neurosci.* **17**, 131–143 (2014).
43. Hanani, M. Satellite glial cells in sensory ganglia: from form to function. *Brain Res. Brain Res. Rev.* **48**, 457–476 (2005).
44. Hanani, M. Satellite glial cells in sympathetic and parasympathetic ganglia: in search of function. *Brain Res. Rev.* **64**, 304–327 (2010).
45. Camell, C.D. *et al.* Inflammasome-driven catecholamine catabolism in macrophages blunts lipolysis during ageing. *Nature* http://dx.doi.org/10.1038/nature24022 (2017).

ONLINE METHODS

General experimental approaches. No samples, mice, or data points were excluded from the reported analyses. Samples were not randomized to experimental groups. Analyses were not performed in a blinded fashion. More detailed information can be found in the **Life Sciences Reporting Summary**.

Antibodies, stain reagents, and drugs. Antibodies were obtained from the following vendors: anti-F4/80–Alexa Fluor 647 (BioLegend, catalog no. 123122, clone BM8), anti–human CD68 (Dako, catalog no. M 0876, clone PG-M1), anti–human NE transporter (NET) (MAb Technologies, catalog no. NET17-1, clone 3-6C1 sc H10), anti-MAOA (Abcam, catalog no. ab126751, clone GR155892-5), anti-TH (Pel-Freez Biologicals, catalog no. P40101-150, lot 16736), anti-GFP (Abcam, catalog no. ab13970, lot GR279236-1), anti-TH (Aves Lab, catalog no. TYH, lot TH1205), anti-GFP (Invitrogen, catalog no. A11120, lot 1563696), anti-GFP (Abcam, catalog no. ab6556, lot GR292567-1), goat anti–chicken IgY (H+L) secondary antibody, Alexa Fluor 488 (Molecular Probes/Thermo Fisher Scientific, catalog no. A-11039, lot 1759025), goat anti–rabbit IgG (H+L) cross-adsorbed secondary antibody, Alexa Fluor 594 (Molecular Probes/Thermo Fisher Scientific, catalog no. A-11012, lot 1704538), anti-Ly6c–eFluor 405 (eBioscience, catalog no. 48-5932-82, clone HK1.4, lot 4306743), anti-CD11c-PE (BD Pharmingen, catalog no. 553802, clone HL3, lot 47030), anti-CD45.2-PE (BioLegend, catalog no. 109808, clone 104.2), anti-CD45.2-FITC (obtained from S. Kimura (Memorial Sloan Kettering Cancer Center); clone 104.2), anti-CD11b-FITC (ATCC, catalog no. TIB-128, clone M1/70), anti-MHCII-Bio (clone M5/114, ATCC, catalog no. TIB-120), SAv-APC/Cy7 (BioLegend, catalog no. 405208, lot B215107), anti-Ki-67-Alexa488 (BD Biosciences, catalog no. 558616, clone B56, lot 7138687), IgG-Alexa488, isotype control (BD Biosciences, catalog no. 557782, lot 7102576), anti-Siglec-F-BV421 (BD Biosciences, catalog no. 562681, lot 7047598), anti-CD68 (Bio-Rad, catalog no. MCA1957GA, clone FA-11), goat anti–rat IgG (H+L) cross-adsorbed secondary antibody, Alexa Fluor 594 (Invitrogen, catalog no. A-11007), goat anti–chicken IgY (H+L), Alexa Fluor 647 (Abcam, catalog no. ab150171), goat anti–rabbit IgG (H+L), Alexa Fluor 488, (Abcam, catalog no. ab150077), goat anti–mouse IgG (H+L), Alexa Fluor 488 (Sigma, catalog no. SAB4600387), anti–mouse IgG (whole molecule), Cy3 (Sigma, catalog no. C0992), rabbit anti-UCP1 (Abcam, catalog no. ab10983, lot GR249119-8), mouse anti-NET (MAb Technologies, catalog no. NET05-2, clone 2-3 B2 sc D7). SYTOX Blue dead cell stain (Molecular Probes/Thermo Fisher Scientific, catalog no. S34857, lot 1851462) was used to exclude dead cells. HCS LipidTOX Deep Red Neutral Lipid Stain (Molecular Probes/Thermo Fisher Scientific, catalog no. H34477) and HCS LipidTOX Red Neutral Lipid Stain (Molecular Probes/Thermo Fisher Scientific, catalog no. H34476) were used to stain lipids.

Acetylcholine chloride, nisoxetine hydrochloride, clorgyline, and NE were purchased from Sigma-Aldrich.

Mice. *Cx3cr1*$^{GFP/+}$ mice (*Cx3cr1*^{tm1Litt}/LittJ; stock no. 008451), *Th-cre* mice (stock no. 008601), *GFP-L10* mice (stock no. 024750), *LysM-cre* mice (stock no. 004781), LSL-*ChR2-YFP* mice (stock no. 012-569), LSL-*tdTomato* mice (stock no. 007909), *ob*/*ob* mice (stock no. 000632), and *Csf1r*-LSL-*DTR* mice (stock no. 024046) were purchased from the Jackson Laboratory (JAX). *NET*$^{P/P}$ (*Slc6a2*$^{-/-}$) mice were kindly provided by M. Hahn (Vanderbilt University). B6 (C57BL/B6J) and B6-CD45.1 mice were purchased from Charles River and were bred and maintained at Instituto Gulbenkian de Ciência. Both males and females were used in this study. Mice were 4–10 weeks old (for details, see the **Life Sciences Reporting Summary**). Animal procedures were approved by the ethics committee of Instituto Gulbenkian de Ciência.

Immunofluorescence and confocal microscopy. Tissues were dissected and fixed in 4% paraformaldehyde for 2 h (at room temperature (RT), with agitation). For images in **Figure 2j**,**k**, we employed frozen sections and the fixation step was followed by cryoprotection in 30% sucrose (Alfa Aesar). 16-µm sections were obtained in a Leica Cryostat CM3050 S. Both frozen sections and whole-mount tissues were incubated in a blocking and permeabilization solution (3% BSA, 2% goat serum, 0.1% Tween, and 0.1% sodium azide in 1× PBS) for 1 h at RT with (whole mounts) or without (frozen sections) agitation. Incubations with primary antibodies were performed overnight at 4 °C with (whole mounts) or without (frozen sections) agitation. The following dilutions of primary antibodies were used: anti-GFP (1:500), anti-TH (1:1,000), anti-SLC6A2 (1:500), anti-MAOA (1:100). Incubation with secondary antibodies was performed for 1–2 h at RT, with or without (in the case of frozen sections) agitation. *Z*-series stacks were acquired on a Leica TCS SP5 confocal inverted microscope. Analysis and quantification of images were performed in Fiji.

***In vivo* two-photon microscopy.** Mice aged 2 months were kept anesthetized with 2% isoflurane. During surgery, body temperature was maintained at 37 °C with a warming pad. After application of local anesthetics (lidocaine), a sagittal incision of the skin was made above the suprapelvic flank to expose the subcutaneous inguinal fat pad. An imaging chamber was custom-built to minimize fat movement. Warm imaging solution (in mM: 130 NaCl, 3 KCl, 2.5 $CaCl_2$, 0.6 $MgCl_2.6H_2O$, 10 HEPES without sodium, 1.2 $NaHCO_3$, 10 glucose, pH 7.45 with NaOH) (37 °C) mixed with a fat dye (LipidTOX) was applied to label adipocytes, maintain tissue integrity, and allow the use of an immersion objective. Imaging experiments were performed under a two-photon laser-scanning microscope (Ultima, Prairie Instruments). Live images were acquired at 8–12 frames per second at depths below the surface ranging from 100–250 mm, using an Olympus 20× 1.0 N.A. water-immersion objective with a laser tuned to a wavelength of 810–940 nm and emission filters at 525/50 nm and 595/50 nm for green and red fluorescence, respectively. Laser power was adjusted to be 20–25 mW at the focal plane (maximally 35 mW), depending on the imaging depth and levels of GFP expression and LipidTOX spread. Analysis and quantification of images were performed in Fiji.

Electron microscopy. Fresh tissue was perfused with 2% paraformaldehyde (Electron Microscopy Services (EMS)) and 0.2% glutaraldehyde (EMS) in 0.1 M phosphate buffer (PB; pH 7.4). After perfusion, fibers were isolated and immersion fixed for 2 h at RT in the same fixative. For quenching of autofluorescence from free aldehydes, nerves were washed with 0.15% glycine (VWR) in PB for 10 min at RT.

Correlative light–electron microscopy. After fixation, fibers were stabilized with 0.1% tannic acid (EMS) and embedded in 2% agarose (Omnipur) before cryoprotection in 30% sucrose (Alfa Aesar) overnight at 4 °C. Embedded samples were placed in optimal cutting temperature (OCT) compound (Sakura) and plunge frozen in liquid nitrogen. 10-µm sections were obtained in a Leica Cryostat CM3050 S and placed on cover glasses coated with 2% (3-aminopropyl) triethoxysilane (Sigma-Aldrich) in acetone. Light microscopy imaging was performed in a Leica SP5 Live microscope after mounting the sections with PB. For electron microscopy processing, samples were washed ten times with PB and post-fixed in 1% osmium tetroxide (EMS) with 1% potassium hexacyanoferrate (Sigma-Aldrich) in PB for 30 min on ice. Dehydration was done in a graded ethanol series of 30%, 50%, 75%, 90%, and 100% ethanol for 10 min each. EPON resin (EMS) was used for embedding. 70-nm serial sections were obtained in a Leica EM UC7 and stained with 1% uranyl acetate and lead citrate for 5 min each. Electron microscopy images were acquired on a Hitachi H-7650 operating at 100 kV.

Single-cell suspension. Tissues were dissected from ten mice. Spleen, brain, visceral fat, and subcutaneous fat were excised and digested for 30 min with collagenase (Sigma) at 37 °C with shaking. Sympathetic nerve fibers were isolated from subcutaneous adipose tissues and digested for 30 min with hyaluronidase (Sigma) at 37 °C with shaking, washed, and further digested with collagenase for 15 min. SCGs were dissected and digested with collagenase for 10 min, washed, and further digested with trypsin (Biowest) for 30 min at 37 °C with shaking. Cell suspensions were filtered through a 70-µm sieve and centrifuged at 450*g* for 5 min.

Flow cytometry. Flow cytometry data were acquired on an LSR Fortessa X-20 SORP (Becton-Dickinson), FACSCalibur (Becton-Dickinson), or CyAn ADP (Beckman Coulter) and analyzed using the FlowJo software package (Tree Star). Macrophages were sorted as live CD45 and F4/80 double-positive cells using a FACSAria IIu high-speed cell sorter (Becton Dickinson) or MoFlo High-Speed Cell Sorter produced by Dako Cytomation (now owned by Beckman Coulter).

Bone marrow chimeras. B6-CD45.1 mice (aged 8–10 weeks), B6 (C57BL/6J) mice (aged 8–10 weeks), and *ob*/*ob* mice (aged 8–10 weeks) were lethally irradiated (900 rad, 3.42 min, ^{137}Cs source) (Gammacell 2000) and reconstituted with bone marrow cells from *Cx3cr1*$^{GFP/+}$ mice (aged 6 weeks), *Slc6a2*$^{-/-}$ mice (aged 6–8 weeks), B6 mice (aged 6–8 weeks), or B6-CD45.1 mice (aged 6–8 weeks). B6-CD45.1 mice and B6 mice were reconstituted with 5×10^6 total bone marrow cells, and *ob*/*ob* mice were reconstituted with 3×10^7 total bone marrow cells. Chimerism was assessed 8 weeks after reconstitution using flow cytometry.

Low-input RNA-seq library preparation. Sequencing libraries were prepared according to the Smart-seq2 method[46] with some modifications. 1,715 ± 115 cells from nerve fibers, 1,534 ± 85 cells from superior cervical ganglia, and 5,000 cells from other tissues (visceral fat, subcutaneous fat, spleen, and brain) were isolated as live CD45$^+$F4/80$^+$ cells in TRIzol (Thermo Fisher) and were used as starting material. RNA was extracted with the Direct-zol MicroPrep kit (Zymo Research) with on-column DNase I treatment. 10 µl of purified RNA was mixed with 5.5 µl of SMARTScribe 5× First-Strand Buffer (Clontech), 1 µl of poly(T) primer for reverse transcription (2.5 µM; 5′-AAGCAGTGGTATCAACGCAGAGTAC(T_{30})VN-3′), 0.5 µl of SUPERase IN (Ambion), 4 µl of dNTP mix (10 mM; Invitrogen), 0.5 µl of dithiothreitol (DTT) (20 mM; Clontech), and 2 µl of betaine solution (5 M; Sigma), and samples were incubated at 50 °C for 3 min. 3.9 µl of first-strand mix, containing 0.2 µl of 1% Tween-20, 0.32 µl of $MgCl_2$ (500 mM), 0.88 µl of betaine solution (5 M; Sigma), 0.5 µl of SUPERase IN (Ambion), and 2 µl of SMARTScribe Reverse Transcriptase (100 U/µl; Clontech), was added, and samples were incubated with one step at 25 °C for 3 min and one step at 42 °C for 60 min. 1.62 µl of template-switch (TS) reaction mix containing 0.8 µl of biotin-TS oligonucleotide (10 µM; biotin-5′-AAGCAGTGGTATCAACGCAGAGTACATrGrG+G-3′), 0.5 µl of SMARTScribe Reverse Transcriptase (100 U/µl; Clontech), and 0.32 µl of SMARTScribe 5× First-Strand Buffer (Clontech) was added, and samples were then incubated at 50 °C for 2 min, 42 °C for 80 min, and 70 °C for 10 min. 14.8 µl of second-strand synthesis, preamplification mix containing 1 µl of preamplification oligonucleotide (10 µM; 5′-AAGCAGTGGTATCAACGCAGAGT-3′), 8.8 µl of KAPA HiFi Fidelity Buffer (5×; KAPA Biosystems), 3.5 µl of dNTP mix (10 mM; Invitrogen), and 1.5 µl of KAPA HiFi HotStart DNA Polymerase (1U/µl; KAPA Biosystems) was added, and samples were amplified by PCR: 95 °C for 3 min, 8 cycles at 98 °C for 20 s, 67 °C for 15 s, and 72 °C for 6 min, and a final extension step at 72 °C for 5 min. The synthesized double-stranded DNA (dsDNA) was purified using Sera-Mag SpeedBeads (Thermo Fisher Scientific) with final concentrations of 8.4% PEG 8000 and 1.1 M NaCl and then was eluted with 13 µl of UltraPure water (Invitrogen). The product was quantified by Qubit dsDNA High Sensitivity Assay Kit (Invitrogen), and libraries were prepared using the Nextera DNA Sample Preparation Kit (Illumina). Tagmentation mix containing 11 µl of 2× Tagment DNA Buffer and 1 µl of Tagment DNA Enzyme was added to 10 µl of purified DNA, and samples were then incubated at 55 °C for 15 min. 6 µl of Nextera Resuspension Buffer (Illumina) was added, and samples were incubated at RT for 5 min. Tagmented DNA was purified using Sera-Mag SpeedBeads (Thermo Fisher Scientific) with final concentrations of 7.8% PEG 8000 and 0.98 M NaCl and then eluted with 25 µl of UltraPure water (Invitrogen). Final enrichment amplification was performed with Nextera primers, adding 1 µl of Index 1 primers (100 µM; N7xx), 1 µl of Index 2 primers (100 µM; N5xx) and 27 µl of NEBNext High-Fidelity 2× PCR Master Mix (New England BioLabs) and then amplifying samples by PCR: 72 °C for 5 min, 98 °C for 30 s, and 8–13 cycles of 98 °C for 10 s, 63 °C for 30 s, and 72 °C for 1 min. Libraries were size selected, quantified by Qubit dsDNA HS Assay Kit (Thermo Fisher Scientific), and pooled and sequenced on a NextSeq 500 (Illumina) for 76 cycles at a depth of 25 to 30 million single-end reads per sample. To normalize for genomic DNA contamination, which occurred in some samples due to incomplete DNA removal during RNA isolation, the average intronic noise per base pair in all intronic regions per gene was calculated. The exonic reads were then normalized by subtracting the background noise per base pair for the complete length of the exonic regions. Genes without introns were not normalized, as these genes are the minority of genes and are typically short (code available at https://github.com/vlink/DNA_contamination/).

Fastq files from sequencing experiments were mapped to the mouse mm10 genome using default parameters for STAR[47]. Mapped data were analyzed with HOMER[48] and custom R and Perl scripts.

Superior cervical ganglion explant cultures. SCGs were removed from mice aged 4–6 weeks under a stereomicroscope and placed in DMEM (Invitrogen, Carlsbad, CA, USA). Ganglia were cleaned from the surrounding tissue capsule and transferred into eight-well tissue culture chambers (Sarstedt, Nümbrecht, Germany) that were previously coated with poly-D-lysine (Sigma-Aldrich, Steinheim, Germany) in accordance with the manufacturer's instructions. Ganglia were then covered with 5 µl of Matrigel (BD Bioscience, San Jose, CA, USA) and incubated for 7 min at 37 °C. DMEM without phenol red (Invitrogen) supplemented with 10% FBS (Invitrogen), 2 mM L-glutamine (Biowest, Nuaillé, France), and nerve growth factor (Sigma-Aldrich) was subsequently added. 12 SCG explant cultures were prepared per condition. SCGs were cultured for a minimum of 24 h before further manipulation. The stimulation protocol in **Figure 3** was performed for 2 h with the following concentrations of drugs: 10 mM acetylcholine chloride, 100 nM nisoxetine hydrochloride, and 100 µM clorgyline.

NE measurements after optogenetic stimulation *ex vivo*. Depolarization of sympathetic neurons in *Th-cre*; LSL-*ChR2-YFP* explant cultures was performed on a Yokogawa CSU-X Spinning Disk confocal microscope using the 488-nm laser line pointing at the region of interest (ROI) for 200 µs. Stimulation was repeated seven times using 40% laser intensity. NE content in the SCG explant culture medium and in sorted CD45$^+$F4/80$^+$ cells was determined by NE ELISA kit (Labor Diagnostika Nord, Nordhorn, Germany, catalog no. BA E-5200). The same procedure was performed for LSL-*ChR2-YFP* control mice.

NE measurements in macrophages from sWAT. CD45.2 (PE)$^+$F4/80 (Alexa Fluor 647)$^+$ cells from sWAT were sorted as live cells and incubated with 2 µM NE for 2 h using the same culture conditions as those used for SCG explant cultures. Afterwards, cells were washed twice with 1× PBS, and NE content was measured by NE ELISA kit (Labor Diagnostika Nord, Nordhorn, Germany, catalog no. BA E-5200).

qPCR. Total RNA from sorted cells was isolated using the RNeasy Plus Micro Kit (Qiagen, catalog no. 50974034). Total RNA from adipose tissues was isolated with the PureLink RNA Mini Kit (Ambion, Life Technologies, catalog no. 12183025). cDNA was reverse transcribed using SuperScript II (Invitrogen) and random primers (Invitrogen). qPCR was performed using SYBR Green (Applied Biosystems) in ABI QuantStudio 7 (Applied Biosystems). The *Gapdh* housekeeping gene was used to normalize samples. We used the following formula to calculate relative expression levels: $RQ = 2^{-\Delta Ct} \times 100 = 2^{-(Ct\ \text{gene of interest} - Ct\ Gapdh)} \times 100$.

The primers used were as follows: *Lpl*-forward, 5′-CAGCTGGGCCTAACTTTGAG-3′; *Lpl*-reverse, 5′-CCTCTCTGCAATCACACGAA-3′; *Pnpla2*-forward, 5′-CACTTTAGCTCCAAGGATGA-3′; *Pnpla2*-reverse, 5′-TGGTTCAG TAGGCCATTCCT-3′; *Gfap*-forward, 5′-CCAGCTTCGAGCCAAGGA-3′; *Gfap*-reverse, 5′-GAAGCTCCGCCTGGTAGACA-3′; *Gap43*-forward, 5′-AGCCAAGGAGGAGCCTAAAC-3′; *Gap43*-reverse, 5′-CTGTCGGGCA CTTTCCTTAG-3′; *Ucp1*-forward, 5′-GTGAAGGTCAGAATGCAAGC-3′; *Ucp1*-reverse, 5′-AGGGCCCCCTTCATGAGGTC-3′; *Slc6a2*-forward, 5′-CAGGCACCTCCATTCTGTTT-3′; *Slc6a2*-reverse, 5′-GCGGCTTGAAGTTGATGATGCTG-3′; *Maoa*-forward, 5′-GCCCAGTA TCACAGGCCAC 3′; *Maoa*-reverse, 5′-GTCCCACATAAGCTCCACCA-3′; *Chrm1*-forward, 5′-CA GTCCCAACATCACCGTCTT-3′; *Chrm1*-reverse, 5′-GAGAACGAAGGAAACCAACCAC-3′; *Chrm2*-forward, 5′-TGTCTCCCAGTCTAGTGCAAGG-3′; *Chrm2*-reverse, 5′-CATTCTGA CCTGACGATCCAAC-3′; *Chrm4*-forward, 5′-GCCTTCATCCTCACCTGGAC-3′; *Chrm4*-reverse, 5′-AGTGGCATTGCAGAGTGCAT-3′; *Chrm5*-forward, 5′-CCA TGGACTGTGGGAAGTCA-3′; Chrm5-reverse, 5′-CAGCGTCC CATGAGGATGTA-3′; *Chrna2*-forward, 5′-CTCCCATCCTGCTTTCCAG-3′; *Chrna2*-reverse, 5′-GTTTGAACAGGCGGTCCTC-3′; *Chrna3*-forward, 5′-GCGAACAGGTCACAGTTTATG-3′; *Chrna3*-reverse, 5′-GCATTTT TCTCTGGGTTTTCA-3′; *Chrna5*-forward, 5′-CGCTCTTCTTCCACACACAA-3′; *Chrna5*-reverse, 5′-TAGGTCCACCGTCTTTCTCG-3′; *Chrna6*-forward, 5′-CTTTGTCACGCTGTCCAT-3′; *Chrna6*-reverse, 5′-GCCTCCT TTGTCTTGTCC-3′; *Chrna7*-forward, 5′-ACAGTACTTCGCCAGCACCA-3′; *Chrna7*-reverse, 5′-AAACCATGCACACCAATTCA-3′; *Chrna9*-forward, 5′-ACAAGGCCACCAACTCCA-3′; *Chrna9*-reverse, 5′-ACCAACCCACTCCTCCTCTT-3′; *Chrna10*-forward, 5′-TCTGACCTCA

doi:10.1038/nm.4422

CAACCCACAA-3′; *Chrna10*-reverse, 5′-TCC TGTCTCAGCCTCCATGT-3′; *Chrnb2*-forward, 5′-GGGCAGGCA CACTATTCTTC-3′; *Chrnb2*-reverse, 5′-TCCAATCCTCCCTCACACTC-3′; *Chrnb3*-forward, 5′-CTCCTCAGACATT GGTTCCAAGG-3′; *Chrnb3*-reverse, 5′-AATGAGG TCAACCATGGT-3′; *Chrnb4*-forward, 5′-TCTGGTTGCCTGACATCGTG-3′; *Chrnb4*-reverse, 5′-GGGTTCACAAAGTACATGGA-3′;*Adrb2*-forward, 5′- GGTTATCGTCCTGG CCATCGTGTTTG-3′; *Adrb2*-reverse, 5′-TGGTTCGTGAAGAAGTCACAGC AAGTCTC-3′; *Th*-forward, 5′-GGTATACGCCACGCTGAAGG-3′; *Th*-reverse, 5′- TAGCCACAGTACCGTTCCAGA-3′; *Tnfa*-forward, 5′- ATGAG CACAGA AAGCATGATC-3′; *Tnfa*-reverse, 5′-TACAGGCTTGTCACTCGAATT-3′; *Il10*-forward, 5′-GCTCTTACTGACTGGCATGAG-3′; *Il10*-reverse, 5′-CGCAG CTCTAG GAGCATGTG-3′; *Il1*-forward, 5′- GAAGAAGAGCCCATCCT CTG-3′; *Il1*-reverse, 5′- TCATCTCGGAGCCTGTAGTG-3′; *Il4ra*-forward, 5′-TGACCTCACAGGAACCCAGGC-3′; *Il4ra*-reverse, 5′-GAACAGGC AAAACAACGGGAT-3′; *Gapdh*-forward, 5′-AACTTTGGCATTGTGGA AGG-3′; *Gapdh*-reverse, 5′-ACACATTGGGGGTAGGAACA-3′.

Functional studies. We measured rectal temperature with an electronic thermometer (Precision) when the mice were housed both at RT and at 4 °C with ND food and water *ad libitum*.

Free fatty acids were measured in blood plasma using the Free Fatty Acid Quantitation Kit (Sigma-Aldrich, catalog no. MAK044-1KT).

Serum levels of NE were determined by NE ELISA kit (Labor Diagnostika Nord, Nordhorn, Germany, catalog no. BA E-5200).

High-fat diet challenge. When B6 mice reached 8 weeks of age, we replaced ND with HFD (Ssniff, Spezialdiäten, Soest, Germany, catalog no. D12492). Analyses in **Figure 4** were performed when mice achieved a 40% increase in body weight after 3 months of a HFD.

Intracellular staining for Ki-67. Cells were surface-stained for 30 min. Subsequently, cells were washed and fixed with fixation and permeabilization buffer (eBioscience) and then permeabilized with permeabilization buffer (eBioscience). Following this process, cells were intracellularly stained with anti-Ki-67 or isotype control.

Histopathological and immunohistochemical analyses. Human and mouse tissues were fixed in buffered formalin, and inclusion in paraffin was done according to standard technical procedures. Histochemical and immunohistochemical studies were performed on formalin-fixed and paraffin-embedded (FFPE) tissue sections. Sections were 2 µm (human ganglia) or 3–6 µm (mouse tissues) thick for H&E or were 4 µm thick for immunohistochemical studies. The following markers were used for immunohistochemistry: aminoethylcarbazole (AEC) and 3,3′-diaminobenzidine (DAB) according to the usual technical procedure for the marker. For the immunohistochemical studies, sections underwent antigenic recovery before incubation with primary antibodies: anti-CD68 (Dako, clone PG-M1; dilution 1:150) anti–human SLC6A2 (MAb Technologies, clone 3-6C1 sc H10; dilution 1:1,000), anti-MAOA (Abcam, clone GR155892-5; dilution 1:50), and anti-UCP1 (Abcam; dilution 1:500). Human tissues were analyzed under an optical microscope (Nikon Eclipse 50i), and iconography microscopic images were captured using a coupled digital camera (DS Camera Control Unit DS-L2). Mouse tissues were analyzed using a Leica DM LB2 microscope, and images were captured with a Leica DFC 250 camera.

Diphtheria toxin–mediated macrophage depletion. We used *LysM-cre*; LSL-*Csf1r-DTR* mice for this experiment and LSL-*Csf1r-DTR* mice as controls. Animals received injections of diphtheria toxin (DT) from *Corynebacterium diphtheria* (Calbiochem) once daily for four consecutive days. The first dose was 500 ng of DT in PBS per 20 g of body weight followed by three doses of 250 ng of DT in PBS per 20 g of body weight. Depletion was assessed by flow cytometry 12 h after the fourth injection. NE levels in adipose tissues were assayed by NE ELISA kit (Labor Diagnostika Nord, Nordhorn, Germany, catalog no. BA E-5200). Protein concentration was determined by the Bradford method.

Statistics. Statistical analyses were performed with GraphPad Prism software (San Diego, CA) using unpaired Student's *t*-test (two-tailed) when two groups were being compared or one-way ANOVA when several groups were being compared. One-way ANOVA was followed by Tukey's multiple-comparisons test, except for the data in **Figure 4b** and **Supplementary Figure 8a**, where it was followed by Bonferroni multiple-comparisons test with one group indicated as a control group. $P < 0.05$ was considered statistically significant. Data are represented as mean ± s.e.m. Sample size was predetermined based on previous studies (for more information, see the **Life Sciences Reporting Summary**). Data displayed normal variance.

Data availability. The RNA-seq data sets are available at GSE103847. The data that support the findings herein presented are available from the corresponding author upon reasonable request. A **Life Sciences Reporting Summary** is available.

46. Picelli, S. *et al.* Smart-seq2 for sensitive full-length transcriptome profiling in single cells. *Nat. Methods* **10**, 1096–1098 (2013).
47. Dobin, A. *et al.* STAR: ultrafast universal RNA-seq aligner. *Bioinformatics* **29**, 15–21 (2013).
48. Heinz, S. *et al.* Simple combinations of lineage-determining transcription factors prime *cis*-regulatory elements required for macrophage and B cell identities. *Mol. Cell* **38**, 576–589 (2010).

nature research

Corresponding Author: Ana Domingos

Date: 7.09.2017

Life Sciences Reporting Summary

Nature Research wishes to improve the reproducibility of the work we publish. This form is published with all life science papers and is intended to promote consistency and transparency in reporting. All life sciences submissions use this form; while some list items might not apply to an individual manuscript, all fields must be completed for clarity.

For further information on the points included in this form, see Reporting Life Sciences Research. For further information on Nature Research policies, including our data availability policy, see Authors & Referees and the Editorial Policy Checklist.

Experimental design

1. Sample size

   Describe how sample size was determined.

   The amount of mouse tissues pooled per sample was determined in order to meet the requirements of applied measurements. For instance, for RNA-seq and gene expression studies tissues from 10 mice were pooled to obtain sufficient amount of cells. For norepinephrine measurements in sorted cells, tissues were pooled from at least 6 mice to meet the assay requirements. All ex-vivo and in-vitro experiments were performed at least three times. For gene expression studies the minimum amount of 2 experiments was employed.
   Sample size in experiments involving mice was estimated based on previous experiments (as optimal for in-vivo evaluation). In the studies involving genetically modified animals group sizes of minimum 3-4 animals were used.

2. Data exclusions

   Describe any data exclusions.

   There was no data exclusion.

3. Replication

   Describe whether the experimental findings were reliably reproduced.

   Findings were reproduced as stated in the figure legends.

4. Randomization

   Describe how samples/organisms/participants were allocated into experimental groups.

   Randomization was not used.

5. Blinding

   Describe whether the investigators were blinded to group allocation during data collection and/or analysis.

   Blinding was not used.

Note: all studies involving animals and/or human research participants must disclose whether blinding and randomization were used.

Nature Medicine: doi:10.1038/nm.4422

6. Statistical parameters

For all figures and tables that use statistical methods, confirm that the following items are present in relevant figure legends (or the Methods section if additional space is needed).

n/a	Confirmed	
☐	☒	The exact sample size (*n*) for each experimental group/condition, given as a discrete number and unit of measurement (animals, litters, cultures, etc.)
☐	☒	A description of how samples were collected, noting whether measurements were taken from distinct samples or whether the same sample was measured repeatedly.
☐	☒	A statement indicating how many times each experiment was replicated
☐	☒	The statistical test(s) used and whether they are one- or two-sided (note: only common tests should be described solely by name; more complex techniques should be described in the Methods section)
☐	☒	A description of any assumptions or corrections, such as an adjustment for multiple comparisons
☐	☒	The test results (e.g. *p* values) given as exact values whenever possible and with confidence intervals noted
☐	☒	A summary of the descriptive statistics, including central tendency (e.g. median, mean) and variation (e.g. standard deviation, interquartile range)
☐	☒	Clearly defined error bars

See the web collection on statistics for biologists for further resources and guidance.

Software

Policy information about availability of computer code

7. Software

Describe the software used to analyze the data in this study.

Fastq files from sequencing experiments were mapped to the mouse mm10 genome using default parameters for STAR 44.
(Dobin, A. et al. STAR: ultrafast universal RNA-seq aligner. Bioinformatics 29, 15–21 (2013))
Mapped data were analyzed with HOMER 45, custom R, and Perl scrpts. (Heinz, S. et al. Simple Combinations of Lineage-Determining Transcription Factors Prime cis-Regulatory Elements Required for Macrophage and B Cell Identities. Mol. Cell 38, 576–589 (2010))

To normalize for genomic DNA contamination, which occurred in some samples due to incomplete DNA removal during RNA isolation, the average intronic noise per base pair in all intronic regions per gene was calculated. The exonic reads were then normalized by subtracting the background noise per base pair for the complete length of the exonic regions. Genes without introns were not normalized, as these genes are the minority of genes and are typically short. (Code available at: https://github.com/vlink/DNA_contamination).

Flow cytometry data was analyzed using FlowJo software package (Tree Star).

Confocal and multiphoton images were analyzed using FIJI software (Schindelin, J.; Arganda-Carreras, I. & Frise, E. et al. (2012), "Fiji: an open-source platform for biological-image analysis", Nature methods 9(7): 676-682, PMID 22743772).

Statistical analysis were performed using GraphPad Prism software (San Diego, CA).

For all studies, we encourage code deposition in a community repository (e.g. GitHub). Authors must make computer code available to editors and reviewers upon request. The *Nature Methods* guidance for providing algorithms and software for publication may be useful for any submission.

Nature Medicine: doi:10.1038/nm.4422

Materials and reagents

Policy information about availability of materials

8. Materials availability

Indicate whether there are restrictions on availability of unique materials or if these materials are only available for distribution by a for-profit company.	All materials used in this study are readily available.

9. Antibodies

Describe the antibodies used and how they were validated for use in the system under study (i.e. assay and species).	anti-F4/80 - Alexa Fluor 647 (BioLegend, cat# 123122, clone BM8, isotype Rat IgG2a, κ), validation: https://www.biolegend.com/en-us/products/alexa-fluor-647-anti-mouse-f4-80-antibody-4074 anti-human CD68 (Dako, cat# M 0876, clone PG-M1), validation: http://www.ihcworld.com/_protocols/antibody_protocols/cd68_m0876_dako.htm anti-human Norepinephrine Tansporter (Mab Technologies, cat# NET17-1, clone 3-6C1 sc H10), validation: http://mabtechnologies.com/categories/product/5-norepinephrine-transporter-human-net17-1 anti-Monoamine Oxidase A (Abcam, cat# ab126751, clone GR155892-5), validation: http://www.abcam.com/monoamine-oxidase-a-antibody-epr7101-ab126751.html anti-TH (Pel-Freez Biologicals, cat# P40101-150, lot 16736), validation: http://www.pelfreez-bio.com/wp-content/uploads/2014/07/74075-PDS-P40101-Tyrosine-Hydroxylase-Antibody-Rabbit-Rev-02.pdf anti-GFP (Abcam, cat # ab13970, lot GR279236-1), validation: http://www.abcam.com/gfp-antibody-ab13970.html Goat anti-Chicken IgY (H+L) Secondary Antibody, Alexa Fluor 488 (Molecular Probes/ Thermo Fisher Scientific, cat# A-11039, lot 1759025), validation: https://www.thermofisher.com/antibody/product/Goat-anti-Chicken-IgY-H-L-Secondary-Antibody-Polyclonal/A-11039 Goat anti-Rabbit IgG (H+L) Cross-Adsorbed Secondary Antibody, Alexa Fluor 594 (Molecular Probes/ Thermo Fisher Scientific, cat# A-11012, lot 1704538), validation: https://www.thermofisher.com/antibody/product/Goat-anti-Rabbit-IgG-H-L-Cross-Adsorbed-Secondary-Antibody-Polyclonal/A-11012 anti-Ly6c-eFluor 405 (eBioscience, cat# 48-5932-82, clone HK1.4, lot 4306743), validation: https://www.thermofisher.com/antibody/product/Ly-6C-Antibody-clone-HK1-4-Monoclonal/48-5932-82 anti-CD11c-PE (BD Pharmingen, cat#553802, clone HL3, lot 47030), validation: http://www.bdbiosciences.com/us/reagents/research/antibodies-buffers/immunology-reagents/anti-mouse-antibodies/cell-surface-antigens/pe-hamster-anti-mouse-cd11c-hl3/p/553802 anti-CD68 (Bio-Rad, cat# MCA1957GA, clone FA-11) , validation: https://www.bio-rad-antibodies.com/mouse-cd68-antibody-fa-11-mca1957.html Goat anti-Rat IgG (H+L) Cross-Adsorbed Secondary Antibody, Alexa Fluor 594 (Invitrogen, cat# A-11007) anti-CD45.2-PE (Biolegend, cat# 109808, clone 104.2), validation: https://www.biolegend.com/it-it/products/pe-anti-mouse-cd45-2-antibody-7 anti-CD45.2-FITC (obtained from Dr. Shoji Kimura from Memorial Sloan-Kettering Cancer Center, New York, NY, clone 104.2, titration results can be provided upon request) anti-CD11b-FITC (ATCC # TIB-128, clone M1/70, titration results can be provided upon request) anti-MHCII-Bio (ATCC # TIB-120, clone M5/114, titration results can be provided upon request) SAv-APC/Cy7 (Biolegend, cat# 405208, lot B215107), validation: https://www.biolegend.com/fr-ch/products/apc-cy7-streptavidin-1471

10. Eukaryotic cell lines

a. State the source of each eukaryotic cell line used. NA

b. Describe the method of cell line authentication used. NA

c. Report whether the cell lines were tested for mycoplasma contamination. NA

d. If any of the cell lines used in the paper are listed in the database of commonly misidentified cell lines maintained by ICLAC, provide a scientific rationale for their use. NA

Animals and human research participants

Policy information about studies involving animals; when reporting animal research, follow the ARRIVE guidelines

11. Description of research animals

Provide details on animals and/or animal-derived materials used in the study.

Mice:
Ob/ob mice (Stock No: 000632, the Jackson Laboratory (JAX)) - males and females, 8-10 weeks old
LSL-ChR2-YFP mice (Stock No: 012-569, JAX) - males and females, 4-6 weeks old mice were used for superior cervical ganglia explant cultures
TH-Cre mice (Stock No: 008601, JAX) - males and females, 4-6 weeks old mice were used for superior cervical ganglia explant cultures and 8-10 weeks old mice were used for subcutaneous adipose tissue imaging purposes
Cx3cr1GFP/+ mice (Cx3cr1tm1Litt/LittJ; Stock No: 008451, JAX) - males and females, 6-10 weeks old
GFPL10 mice (Stock No: 024750, JAX) - males and females, 8-10 weeks old
LysM-Cre mice (Stock No: 004781, JAX)- males and females, 8-10 weeks old
LSL-tdTomato mice (Stock No: 007909, JAX) - males and females, 8-10 weeks old
NET P/P (Slc6a2-/-) mice were kindly provided by Maureen Hahn from the University of Vanderbilt (Shirey-Rice, J. K. et al. Norepinephrine transporter variant A457P knock-in mice display key features of human postural orthostatic tachycardia syndrome. Dis. Model. Mech. 6, 1001–1011 (2013)) - males and females, 4-6 weeks old mice were used for superior cervical ganglia cultures, 6-8 weeks old mice were used for bone marrow chimeras
C57BL/B6J and B6-CD45.1 mice were purchased from Charles River, bred and maintaned at Instituto Gulbenkian de Ciência- males and females, 4-10 weeks old.
CSF1R-LSL-DTR (Stock No: 024046, JAX) - males and females, 8-10 weeks old

Animal procedures were approved by the ethics committee of Instituto Gulbenkian de Ciência

Policy information about studies involving human research participants

12. Description of human research participants

Describe the covariate-relevant population characteristics of the human research participants.

We obtained human specimens from a biobank collection of paraffin embedded tissues housed at the local university hospital (Hospital Santa Maria, Lisbon, Portugal). These SNS samples were removed during sympathectomy and/or gangliotomy surgeries, and correspond to excisional biopsies of SNS or ganglia in the thoracolumbar region.

Nature Medicine: doi:10.1038/nm.4422

nature research

Corresponding Author: Ana Domingos

Date: 7.09.2017

Flow Cytometry Reporting Summary

Form fields will expand as needed. Please do not leave fields blank.

Data presentation

For all flow cytometry data, confirm that:

☒ 1. The axis labels state the marker and fluorochrome used (e.g. CD4-FITC)

☒ 2. The axis scales are clearly visible

☒ 3. All plots are contour plots with outliers or pseudocolor plots

☒ 4. A numerical value for number of cells or percentage (with statistics) is provided

Methodological details

5. Describe the sample preparation.

After perfusion of mice with PBS, tissues were dissected from 10 mice. Spleen, brain, visceral fat and subcutaneous fat were excised and digested for 30 minutes with collagenase (Sigma) at 37ºC with shaking. Spleen was subjected to red blood cell lysis. Sympathetic nerve fibers were isolated from subcutaneous adipose tissues and digested for 30 minutes with Hyaluronidase (Sigma) at 37ºC with shaking, washed and further digested with collagenase for 15 minutes. SCG were dissected and digested with collagenase for 10 minutes, washed and further digested with trypsin (Biowest) for 30 minutes at 37ºC with shaking. Cell suspensions were filtered through a 70 microns mesh cell strainer and centrifuged at 450 xg for 5 minutes.

6. Identify the instrument used for data collection.

LSR Fortessa X-20 SORP from Becton-Dickinson
Cyan ADP from Beckman Coulter
FACSCalibur from Becton Dickinson
FACSAria IIu High Speed Cell Sorter from Becton Dickinson
MoFlo High-Speed Cell Sorter produced by Dako Cytomation (now owned by Beckman Coulter)

7. Describe the software used to collect and analyze the flow cytometry data.

For LSR Fortessa the software to collect data is BD FACSDiva™ 8 software
For Cyan ADP from Beckman Coulter the software to collect data is Summit
For FACSCalibur from Becton Dickinson the software to collect data is CellQuest
For FACSAria IIu High Speed Cell Sorter from Becton Dickinson the software to collect data is BD FACSDiva™ 8 software
For MoFlo High-Speed Cell Sorter produced by Dako Cytomation (now owned by Beckman Coulter) the software to collect data is Summit
The software used to analyze all flow cytometry data was FlowJo

8. Describe the abundance of the relevant cell populations

After sorting CD45+F4/80+ cell populations, the positive fraction

Nature Medicine: doi:10.1038/nm.4422

within post-sort fractions.

was passed through the cell sorter machine in order to determine the percentage of positive cells. The percentage of CD45+F4/80+ cell populations was in all cases between 97-99%.

9. Describe the gating strategy used.

First we gated in FSC/SSC plots, then we eliminated duplets by gating on FSC-A/FSC-W, after which we eliminated dead cells. In live cells we gated on CD45+ cells and sorted CD45+F4/80+, so the double positive population is obtained.

Tick this box to confirm that a figure exemplifying the gating strategy is provided in the Supplementary Information. ☒

Nature Medicine: doi:10.1038/nm.4422